

# Optimal Control and Leading-Order Thin-Foil Universality for RTI-Limited Radiation-Pressure Acceleration

Sunil Rao<sup>1,\*</sup>

<sup>1</sup>*Independent Researcher*<sup>†</sup>

(Dated: August 23, 2025)

We present an internally consistent analytical framework within the thin-foil approximation  $\gamma^2 + 2\nu_{\text{eff}}k^2\gamma = ak - Tk^3$  for mitigating Rayleigh–Taylor-like instability (RTI) during radiation-pressure acceleration (RPA). Analytical results include: (i) a universality collapse of the linear growth spectrum using the cubic viscous scale  $k_{\nu,3} = (a/\nu_{\text{eff}}^2)^{1/3}$ ; (ii) a measure-theoretic reduction to two-point (CP/LP) programs and a single-switch optimality result under an inverse-Faraday memory state; (iii) tight Pareto frontiers and an information-theoretic “price of impulse”; and (iv) minimax robustness and delay-robust edge-of-transparency (EoT) tracking. The physical closures for  $\nu_{\text{eff}}$  and  $\sigma_s$  are stated explicitly, calibrated against facility-specific priors, and all performance guarantees are carried through with robustness bounds. *Within the thin-foil dispersion  $\gamma^2 + 2\nu_{\text{eff}}k^2\gamma = ak - Tk^3$  and for slender, near-opaque operation*, we prove an exact spectrum normalization using the cubic viscous scale  $k_{\nu,3}$  and a unique similarity number  $\Phi_3$ . The normalization is exact for the base model and *remains leading-order with quantified error* on  $x \in [\varepsilon, 1 - \varepsilon]$  for any fixed  $\varepsilon \in (0, 1)$ ; a vanishing neighborhood of the cutoff  $x \rightarrow 1$  is excluded because higher-order finite-thickness and dispersive terms can compete. We report thresholds for the R4 regime ( $kd \gtrsim 0.2\text{--}0.3$ ) and carry explicit  $O(\xi^2, (k_T\ell)^2)$  error bands in all overlays. Results are valid on  $x \in [\varepsilon, 1 - \varepsilon]$  with quantified  $O(\xi^2)$  corrections near cutoff.

PACS numbers: 52.38.Kd, 52.35.Py, 02.30.Yy, 05.40.Ca

**Model validity domain.** Results hold for thin foils  $\epsilon = d/L < 0.3$ , near-opaque operation  $\Theta \lesssim 1$ , linear perturbations  $|\eta|/\lambda_0 < 0.1$ , and  $\xi = kd \lesssim 0.3$ . The normalized spectrum is exact for the base dispersion and remains leading-order on  $x \in [\varepsilon, 1 - \varepsilon]$ ; close to cutoff  $x \rightarrow 1$ , the  $O(\xi^2, (k_T\ell)^2)$  corrections in Eq. (44) can dominate.

Two path functionals summarize performance:

$$J_0 = \int_0^\tau a(u(t)) dt \quad (\text{final ion impulse}), \quad (1)$$

$$X = \int_0^\tau \gamma_{\text{max}}(u(t)) dt \quad (\text{integrated stability cost}). \quad (2)$$

In the linear window, a ripple amplitude obeys  $|\eta(\tau)| \approx |\eta(0)|e^X$ .

The thin-foil RTI dispersion (derived in Sec. II) reads, to  $O(\epsilon^2)$  with  $\epsilon = d/L \ll 1$ ,

$$\gamma^2 + 2\nu_{\text{eff}}k^2\gamma = ak - Tk^3, \quad T = \frac{\sigma_s}{\rho}, \quad (3)$$

where  $\nu_{\text{eff}}$  is an effective (kinematic) viscosity (collisional + RR + magnetized contributions),  $\sigma_s$  is a curvature (capillary-like) modulus,  $\rho$  is mass density, and  $T$  has units  $L^3T^{-2}$ .

## I. NOTATION AND PHYSICAL CONTEXT

### A. Controls, costs, and states

We consider a light-sail (ultrathin foil) driven over  $t \in [0, \tau]$  by a laser field with *control*

$$u(t) = (\Pi(t), I(t)) \in [0, 1] \times [0, I_{\text{max}}],$$

where  $\Pi$  is polarization ellipticity ( $\Pi = 0$  for linear polarization, LP;  $\Pi = 1$  for circular polarization, CP) and  $I$  is intensity. The instantaneous longitudinal *acceleration* is  $a(u)$  and the modal *linear RTI growth rate* is  $\gamma(k; u)$ ; we denote  $\gamma_{\text{max}}(u) = \max_k \gamma(k; u)$ . Circular polarization reduces electron heating and favors radiation-pressure acceleration (RPA) or light-sail (LS) regimes [1–4].

### B. Dimensional analysis and symbols (20+ parameters)

We normalize in SI units and, when useful, indicate the base dimensions  $[M], [L], [T], [Q]$ . The table collects the parameters used throughout.

*Symbols and densities.* We reserve  $\rho$  for *bulk mass density* and  $\Sigma$  for *areal density*. The curvature scale is  $T \equiv \sigma_s/\rho$  and the acceleration is  $a = 2RI/(\Sigma c)$ . To avoid collision with  $T$ , the edge-of-transparency controller uses a time constant  $\tau_\zeta$  (Sec. VIII).

\* sunilkgao@gmail.com

† <https://orcid.org/0009-0009-3337-5726>

TABLE I. Key symbols and dimensions. Overbars denote cycle averages; brackets give base dimensions and SI units.

Symbol	Meaning	Dimensions	SI units
$I$	Laser intensity	$[M T^{-3}]$	$\text{W m}^{-2}$
$\lambda_0, \omega_0 = 2\pi c/\lambda_0, k_0 = \omega_0/c$	Wavelength, ang. frequency, wavenumber	$[L], [T^{-1}], [L^{-1}]$	$\text{m}, \text{s}^{-1}, \text{m}^{-1}$
$a_0 = \frac{eE_0}{m_e c \omega_0}$	Normalized vector potential	$[-]$	$[-]$
$\Pi \in [0, 1]$	Ellipticity (0=LP, 1=CP)	$[-]$	$[-]$
$\theta_{\text{inc}}$	Incidence angle	$[-]$ (rad)	rad
$\mathcal{R}, \mathcal{A}$	Reflectivity, absorptivity (spin absorption fraction $A$ )	$[-]$	$[-]$
$c$	Speed of light	$[L T^{-1}]$	$\text{m s}^{-1}$
$e, m_e, m_i$	Electron charge, electron/ion masses	$[Q], [M], [M]$	C, kg, kg
$r_e = \frac{e^2}{4\pi\epsilon_0 m_e c^2}$	Classical electron radius	$[L]$	m
$\sigma$	Areal mass density	$[M L^{-2}]$	$\text{kg m}^{-2}$
$\rho, d$	Bulk density, thickness	$[M L^{-3}], [L]$	$\text{kg m}^{-3}, \text{m}$
$\epsilon = d/L$	Slenderness (thickness/lateral scale)	$[-]$	$[-]$
$\nu_{\text{eff}}$	Effective kinematic viscosity	$[L^2 T^{-1}]$	$\text{m}^2 \text{s}^{-1}$
$\sigma_s$	Curvature (capillary) modulus	$[M T^{-2}]$	$\text{N m}^{-1}$
$T = \sigma_s/\rho$	Curvature scale	$[L^3 T^{-2}]$	$\text{m}^3 \text{s}^{-2}$
$a$	Sail acceleration	$[L T^{-2}]$	$\text{m s}^{-2}$
$\gamma(k), \gamma_{\text{max}}$	RTI growth rate (mode $k$ ), peak growth	$[T^{-1}]$	$\text{s}^{-1}$
$k, k_T = \sqrt{a/T}$	Wavenumber, tension scale	$[L^{-1}]$	$\text{m}^{-1}$
$k_{\nu,3} = (a/\nu_{\text{eff}}^2)^{1/3}$	Cubic viscous scale	$[L^{-1}]$	$\text{m}^{-1}$
$\Phi_3 = k_T/k_{\nu,3}$	Viscous similarity number	$[-]$	$[-]$
$n_e, n_c$	Electron density, critical density	$[L^{-3}]$	$\text{m}^{-3}$
$\langle \gamma_e \rangle$	Cycle-averaged electron Lorentz factor	$[-]$	$[-]$
$\Theta = \frac{n_c \langle \gamma_e \rangle}{n_e}$	Transparency number	$[-]$	$[-]$
$\chi_e$	QED quantum parameter	$[-]$	$[-]$
$B_x, \Omega_c = eB_x/m_e$	Magnetization (IFE), cyclotron freq.	$[M T^{-2} Q^{-1}], [T^{-1}]$	T, $\text{s}^{-1}$
$\alpha, \tau_B$	IFE gain, magnetization time constant	$[B T^{-1}], [T]$	$\text{T s}^{-1}, \text{s}$
$\zeta$	Edge-of-transparency ratio (Sec. VIII)	$[-]$	$[-]$
$r_a, r_\gamma$	CP/LP ratios for $a, \gamma_{\text{max}}$	$[-]$	$[-]$
$\mathcal{M}_k$	Mode-killer leverage	$[-]$	$[-]$

**Reader's Guide.** For efficient navigation: (i) *Theory focus*—read Secs. II.A–B (model), III (exact collapse), and IV (bang-bang theorems); (ii) *Control focus*—prioritize Secs. IV–V (Pontryagin and Pareto), VIII (EoT tracking); (iii) *Validation focus*—see Sec. III.F (extraction protocol), Fig. 1 (overlay), Table II (calibration); (iv) *Robustness focus*—review Secs. VI–VII (stochastic bounds, minimax); (v) *Design focus*—jump to Sec. IX (mode-killer) and Table III (performance map). Key equations: dispersion (12), collapse (35)–(38), single-switch (57), Pareto slope (62), EoT tracking (98).

### C. First-principles scaling laws (engineer-ready)

*a. (S1) Radiation pressure acceleration.* Near normal incidence in the opaque limit,

$$a(\Pi, I) = \frac{2 \mathcal{R}(\Pi, \Theta)}{c} \frac{I}{\sigma} \cos^2 \theta_{\text{inc}} \times f_T(\Theta), \quad (4)$$

where  $f_T$  accounts for proximity to the relativistic transparency threshold (precise form in Sec. II.D). For most design calculations we take  $\theta_{\text{inc}} \approx 0$  and  $f_T \simeq 1$  at the target guardband.

b. (S2) *RTI tension and viscous scales.* From (3), the natural scales are

$$\begin{aligned} k_T &= \sqrt{\frac{a}{T}}, \\ k_{\nu,3} &= \left( \frac{a}{\nu_{\text{eff}}^2} \right)^{1/3}, \\ \Phi_3 &= \frac{k_T}{k_{\nu,3}}. \end{aligned} \quad (5)$$

Inviscid ( $\nu_{\text{eff}} \rightarrow 0$ ) growth peaks at  $k^\circ = \frac{1}{\sqrt{3}} k_T$  with  $\gamma_{\text{max}}^\circ = \sqrt{\frac{2}{3\sqrt{3}}} \sqrt{ak_T}$ . The *exact* spectrum for all  $\nu_{\text{eff}}$  is given by the collapse in Sec. III.

c. (S3) *Magneto-viscous scaling (IFE/RR).* Inverse Faraday magnetization obeys  $\dot{B}_x = \alpha \Pi - B_x/\tau_B$ ; the magnetized contribution to viscosity scales as

$$\nu_{\text{RR}}^{\text{IF}} \sim C_{\text{IF}} \frac{c^2}{\omega_{pe}^2} \omega_0 \left( \frac{\Omega_c}{\omega_0} \right)^2 \propto B_x^2, \quad (6)$$

while the RR-quiver contribution scales at high  $a_0$  as  $\nu_{\text{RR}}^{\text{QM}} \propto a_0^4$  (Sec. II). Both raise  $\nu_{\text{eff}}$ , hence increase  $\Phi_3$  and suppress growth. (Here  $c^2/\omega_{pe}^2$  is a length-squared scale; SI units check in Sec. II.C.c.)

d. (S4) *Edge-of-transparency (EoT) penalty.* When approaching the relativistic transparency regime [5], with a transparency ratio  $s(t) = \zeta(t)/a_0(t)$  and guardband  $s \geq 1 + \varepsilon$ , optimal tracking (Sec. VIII) yields

$$\begin{aligned} a &\propto \frac{a_0^2}{\zeta} = \frac{a_0}{1 + \varepsilon}, \\ X &\propto \int_0^\tau \gamma_{\text{max}} dt \sim \int_0^\tau \sqrt{ak_T} dt \propto \int_0^\tau \frac{a_0}{\sqrt{\zeta}} dt. \end{aligned} \quad (7)$$

Thus the EoT guardband appears with a square-root penalty in the growth cost.

#### D. Similarity parameters beyond classical groups

We list the dimensionless groups that organize the physics and design:

- **Viscous-tension ratio:**  $\Phi_3 = k_T/k_{\nu,3}$  (controls the exact collapse; Sec. III).
- **Transparency number:**  $\Theta = n_c \langle \gamma_e \rangle / n_e$  (opaque if  $\Theta \ll 1$ , semi-transparent near  $\Theta \simeq 1$ ).
- **Magneto-viscous number:**  $\mathcal{M}_\nu \equiv \beta(\Omega_c/\omega_0)^2$  (RR-IF enhancement of  $\nu_{\text{eff}}$ ).
- **Ablation number:**  $\mathcal{A} \equiv p_{\text{abl}} \sigma c / (2RI)$  (ratio of ablation to photon radiation pressure).
- **Slenderness and thickness:**  $\epsilon = d/L \ll 1$ ,  $\xi = kd$  (finite-thickness correction via  $g(\xi) = \tanh \xi/\xi$ ).
- **IFE Floquet number:**  $\mathcal{F} \equiv \Omega \tau_B$  (dither frequency normalized by magnetization time; Sec. X).

- **CP efficiency ratios:**  $r_a = a_{\text{CP}}/a_{\text{LP}}$ ,  $r_\gamma = \gamma_{\text{max,CP}}/\gamma_{\text{max,LP}}$ .
- **Pareto slope and price:**  $\kappa = (1 - r_\gamma)/(1 - r_a)$  and dual slope  $\lambda = -\partial_J X_{\text{min}}$  (Sec. V).
- **Mode-killer leverage:**  $\mathcal{M}_k = (\partial \sigma_s / \partial d) \delta d / (\rho a / k^2)$  for structured/engineered targets [6–8] (Sec. IX).
- **Noise-to-drift ratio (per mode):**  $\mathcal{R}_k = \Sigma_k / \Gamma_k^2$  (governs stochastic failure tails; Sec. VI).

#### E. Five canonical experimental regimes (dimensionless map)

We delineate operating regimes by the triplet  $(\Phi_3, \Theta, \mathcal{M}_\nu)$  and geometry  $(\epsilon, \xi)$ :

- R1: LP-opaque, weak viscosity.:**  $\Theta \ll 1$ ,  $\Phi_3 \ll 1$ ,  $\mathcal{M}_\nu \approx 0$ ,  $\xi \ll 1$ . Inviscid tension controls; growth near  $k_T/\sqrt{3}$ ; CP gives modest improvement unless  $r_\gamma \ll r_a$ .
- R2: CP-opaque, magneto-viscous.:**  $\Theta \ll 1$ ,  $\Phi_3 = O(1)$  from RR/IFE,  $\mathcal{M}_\nu = O(1)$ . CP substantially lowers  $\gamma_{\text{max}}$  with small impulse penalty ( $\kappa \gg 0$ ).
- R3: Edge-of-transparency.:**  $\Theta \simeq 1 \pm \delta_\Theta$ ,  $s = \zeta/a_0 \geq 1 + \varepsilon$  enforced; use delay-robust  $\zeta$  tracking (Sec. VIII). Finite-thickness and preplasma corrections enter.
- R4: Dispersive finite-thickness.:**  $\xi = kd \gtrsim 0.3$ . Use  $g(\xi)$  in the  $ak$  term; peak shifts to lower  $k$ ; mode-killer design must include  $\partial \sigma_s / \partial d$  at the actual  $d$ . **Thresholds for R4.** We find the finite-thickness term becomes order-controlling around  $kd \simeq 0.2$ – $0.3$  in the compact- $x$  window (Sec. III.C, Eq. (44)); beyond this, we report normalized curves with shaded  $O(\xi^2)$  error bands (Fig. 1b).
- R5: Strong RR/QED seeding.:**  $\chi_e \gtrsim 10^{-1}$ ; RR emission and pair bursts contribute to  $\sigma_k^2$  and jump tails (Sec. VI); robustness requires Pareto and mini-max scheduling (Secs. V,VII).

#### F. CP/LP/hybrid “phase diagram” (selection regions)

Define the monotonicity margin

$$\Delta_\Pi \equiv \frac{1}{3} \partial_\Pi \ln \sigma_s - \partial_\Pi \ln a, \quad (8)$$

evaluated at  $I = I_{\text{max}}$  and fixed  $(\Phi_3, \Theta, \mathcal{M}_\nu, \xi)$ . From Sec. II,  $\Delta_\Pi > 0$  suffices for  $\partial_\Pi \gamma_{\text{max}} < 0$  (*CP more stable*). Combine with the impulse penalty  $r_a < 1$  and stability gain  $r_\gamma < 1$  to define

$$\kappa = \frac{1 - r_\gamma}{1 - r_a}.$$

Then:

- **CP region (C):**  $\Delta_{\Pi} > \eta$  and either  $r_a \geq 1$  (no impulse penalty, all-CP) or  $r_a < 1$  but the required impulse  $J_0$  satisfies  $J_0 \leq a_{\text{CP}}\tau$  (feasible all-CP).
- **Hybrid region (H):**  $\Delta_{\Pi} > -\eta$  but  $J_0 > a_{\text{CP}}\tau$ ; the optimal policy is a single CP→LP switch with CP fraction  $p = \delta/(1 - r_a)$  and frontier slope  $\kappa$  (Sec. V).
- **LP region (L):**  $\Delta_{\Pi} < -\eta$  (CP gives too little stability per impulse), or strong ablation  $\mathcal{A} \gg 1$  destroys the CP benefit. LP@ $I_{\text{max}}$  is optimal.

Here  $\eta > 0$  is a small design tolerance absorbing modeling error/uncertainty (see Sec. VII). In practice, the diagram can be plotted over  $(\Phi_3, \Theta)$  with contours of  $\kappa$  and feasibility  $J_0 \leq a_{\text{CP}}\tau$ .

*Roadmap.* Sec. 2 derives the thin-foil model and closures (with bounds); Sec. 3 proves the exact collapse; Sec. 4–5 develop the optimal control and Pareto frontiers; Sec. 6–7 give stochastic and minimax robustness; Sec. 8–9 present control/design laws; brief extensions are summarized in Sec. 10–12.

**Assumptions, scope, and limitations.** All exact statements hold *within* the thin-foil model  $\gamma^2 + 2\nu_{\text{eff}}k^2\gamma = ak - Tk^3$  with  $\epsilon = d/L \ll 1$ , finite-thickness  $\xi = kd \lesssim 0.3$ , near-normal incidence, and opaque/near-opaque operation ( $\Theta \lesssim 1$ ) such that parametric instabilities do not set the growth scale. The collapse is exact for this model and persists at leading order under small  $T(k), \nu(k)$  dispersive corrections. Optimality relies on monotonicity  $\partial_I \gamma_{\text{max}} \geq 0$ ,  $\partial_{\Pi} \gamma_{\text{max}} \leq 0$  a.e. in the opaque window; failures may occur near relativistic transparency or strong ablation. On such measurable subsets  $\mathcal{T}$  we revert to LP (threshold fallback in Sec. V) while retaining feasibility and global bounds. Quantitative predictions require calibrating  $(C_{\text{QM}}, C_{\text{IF}}, \alpha, \tau_B)$ ; robustness to these priors is carried through via dual/Lipschitz bounds (Sec. VII). Nonlinear RTI and 3D coupling are not modeled; validation targets are specified in Sec. XE.

**Uniformity domain.** All normalized-spectrum identities hold uniformly on  $x \in [\epsilon, 1 - \epsilon]$  with  $\epsilon \in (0, 1)$ ; a vanishing neighborhood of  $x = 1$  is excluded because  $S(x) = x(1 - x^2) \rightarrow 0$  makes  $O(\xi^2)$ ,  $O((k\ell)^2)$  corrections comparable (Sec. III.C, Eq. (44)).

*Related work and contributions.* Classical RPA/LS scalings and RTI phenomenology are reviewed in [2–4]; our new elements are: (i) an *exact* normalization of the thin-foil dispersion with the cubic viscous scale  $k_{\nu,3}$  and a *unique* similarity number  $\Phi_3$  (Theorems 2 & 5); (ii) measure-theoretic extremality  $\Rightarrow$  support  $\leq 2$  and a *single* CP→LP switch when IFE memory is present (Theorems 6, 10, 13); (iii) Pareto frontiers with a dual-slope identity linking impulse to risk exponents (Sec. V–VI); (iv) delay-independent EoT tracking with closed-form ISS bounds (Sec. VIII); (v) mode-killing inverse design with tolerances (Sec. IX). We explicitly state the limits of the base model (Sec. II, III.C) and carry uncertainty

via minimax bounds (Sec. VII). Stochastic RR/QED and pair bursts enter through a jump-diffusion of the log-amplitude  $X_k$  (Sec. VI, Eqs. (80)–(90)), tying into the Pareto ‘price of impulse’ identity (Eq. (92)).

## II. MODEL ASSUMPTIONS: RIGOROUS REDUCTION, CLOSURES, AND ROBUSTNESS

This section establishes a first-principles thin-foil reduction from Vlasov–Maxwell with an explicit small parameter  $\epsilon = d/L \ll 1$ , derives the RTI dispersion with quantified  $O(\epsilon^2)$  truncation, presents radiation-reaction (RR) closures with correct high- $a_0$  scaling, provides correction factors (transparency, incidence, thickness, preplasma, ablation), and proves monotonicity and robustness properties (including near-necessity a.e. and dual Lipschitz bounds).

### A. Geometry, ordering, and the depth integration step

Let the foil occupy the moving slab  $\mathcal{S}_t$  of thickness  $d$  about its mid-surface, with lateral scale  $L$  and  $\epsilon = d/L \ll 1$ . Small slope:  $\|\nabla_{\perp} \eta\|_{\infty} = O(\epsilon)$ . The unit normal and curvature are

$$= (0, 0, 1) + O(\epsilon), \quad \kappa = -\nabla_{\perp}^2 \eta + O(\epsilon^2).$$

The Cauchy momentum equation for total stress  $\mathbf{T} = \rho v v + \mathbf{T}^{\text{kin}} - \mathbf{T}^{\text{EM}}$  reads

$$\partial_t(\rho v) + \nabla \cdot \mathbf{T} = 0. \quad (9)$$

*a. Explicit EM surface split (depth integration).* Integrate (9) over  $\mathcal{S}_t$  and apply the divergence theorem to the electromagnetic part. Denoting by  $n$  the up/down face normal and by  $m$  the outward lateral unit normal on  $\partial \mathcal{S}_t^{\text{lat}}$ , we have the identity

$$\int_{\mathcal{S}_t} \nabla \cdot \mathbf{T}^{\text{EM}} dV = [\mathbf{T}^{\text{EM}} n]_{x=d/2}^{x=-d/2} - \int_{\partial \mathcal{S}_t^{\text{lat}}} \mathbf{T}^{\text{EM}} m d\Gamma, \quad (10)$$

where the *lateral mantle term* scales like  $A_{\text{lat}} = O(d \|\nabla_{\perp} \eta\| L) = O(\epsilon^2)$  of the planform area, hence contributes  $O(\epsilon^2)$  compared to the top–bottom face term. Projecting (9) onto  $n$ , integrating across  $x \in [-d/2, d/2]$ , and linearizing the kinetic stress leads to

$$\begin{aligned} \sigma \partial_t^2 \eta &= [\mathbf{T}^{\text{EM}} : (nn)]_{x=d/2}^{x=-d/2} \\ &\quad - \nabla_{\perp} \cdot \left( \int_{-d/2}^{d/2} \mathbf{T}^{\text{kin}} : (nt_{\alpha}) dx \right) t_{\alpha} \\ &\quad + O(\epsilon^2), \end{aligned} \quad (11)$$

with areal mass  $\sigma = \int_{-d/2}^{d/2} \rho dx$  and tangents  $t_{\alpha}$ .

*Quantified  $O(\epsilon^2)$  remainder.* Let  $R_{\epsilon^2}$  denote the neglected terms in (11) after linearization and small-slope closure. For smooth surfaces with  $\|\nabla_{\perp}\eta\|_{\infty} = O(\epsilon)$  and  $kd = \xi$ , one can bound

$$\|R_{\epsilon^2}\| \leq C_1 \epsilon^2 ak + C_2 \epsilon^2 Tk^3, \quad (12)$$

with  $C_{1,2} = O(1)$  depending on regularity constants. We enforce  $\xi = kd \leq 0.3$  throughout figures and examples, keeping the truncation  $< 10\%$  of the leading terms.

*b. Constitutive linearization and dispersion.* The EM normal stress jump yields the radiation pressure  $P_{\text{rad}}$ . The kinetic stress produces a curvature term with modulus  $\sigma_s = \int (\Pi_{\perp}^{(0)} + \Pi_B^{(0)}) dx > 0$  and a kinematic viscosity  $\nu_{\text{eff}}$ . Seeking  $\eta \sim e^{iky + \gamma t}$ , we obtain, to  $O(\epsilon^2)$ ,

$$\gamma^2 + 2\nu_{\text{eff}} k^2 \gamma = ak - Tk^3, \quad T = \frac{\sigma_s}{\rho}, \quad a = \frac{P_{\text{rad}}}{\sigma}. \quad (13)$$

Equation (13) is the thin-foil RTI dispersion used throughout.

*How  $\Pi$  affects  $\sigma_s$ .* Circular polarization suppresses stochastic heating and can build a quasi-static magnetic pedestal (inverse Faraday), which steepens the density and pressure gradients at the interface. In the thin-sheet reduction this appears as an increased curvature modulus  $\sigma_s$  (effective surface tension) from the kinetic-magnetic stress. A practical calibration is: (i) run LP and CP at the same  $(I, n_e, d)$ ; (ii) extract  $(k_{\text{peak}}, \gamma_{\text{peak}})$ ; (iii) invert to  $(k_T, \Phi_3)$  via the exact collapse; (iv) solve for  $T$  and hence  $\sigma_s = \rho T$ . The CP/LP ratio  $\sigma_s^{\text{CP}}/\sigma_s^{\text{LP}} > 1$  in the opaque regime is the relevant input to the control law.

## B. Radiation pressure and the Landau–Lifshitz RR force

Near normal incidence ( $\theta_{\text{inc}} \ll 1$ ) in the opaque limit,

$$a(\Pi, I) = \frac{2\mathcal{R}(\Pi, \Theta)}{c} \frac{I}{\sigma} \cos^2 \theta_{\text{inc}} \times f_T(\Theta), \quad (14)$$

where  $f_T$  (defined below) captures proximity to transparency. Radiation reaction is modeled by the Landau–Lifshitz (LL) force (SI units, field-derivative terms negligible for a quasi-monochromatic drive)

$$\mathbf{F}_{\text{RR}} = \frac{2e^3}{3m_e c^3} \gamma \times \left[ \left( \mathbf{E} + \frac{\mathbf{v}}{c} \times \mathbf{B} \right)^2 - \frac{1}{c^2} (\mathbf{E} \cdot \mathbf{v})^2 \right] \frac{\mathbf{v}}{c^2}, \quad (15)$$

whose cycle-averaged power and momentum flux underpin the closures below (see, e.g., Refs. Di Piazza 2012; Gonoskov 2022).

## C. Closures for $\nu_{\text{eff}}$ : RR–quiver mixing (QM) and RR–inverse Faraday (IF)

We write

$$\nu_{\text{eff}} = \nu_{\text{coll}} + \nu_{\text{turb}} + \nu_{\text{RR}}^{\text{QM}} + \nu_{\text{RR}}^{\text{IF}}, \quad (16)$$

and derive the RR contributions with correct high- $a_0$  scaling. (Calibration constants  $C_{\text{QM}}, C_{\text{IF}} = O(1)$  absorb geometry and averaging.)

*a. Closure A (RR–QM): mixing length and decorrelation rate.* Relativistic plasma frequency  $\omega'_{pe} = \omega_{pe}/\sqrt{\langle \gamma_e \rangle}$  gives a skin depth

$$\delta_R = \frac{c}{\omega'_{pe}} = \frac{c}{\omega_{pe}} \sqrt{\langle \gamma_e \rangle}, \quad (17)$$

so we take the mixing length  $L_m = \delta_R$ . For CP,  $\langle \gamma_e \rangle \simeq \sqrt{1 + a_0^2}$ , hence

$$L_m = \frac{c}{\omega_{pe}} (1 + a_0^2)^{1/4}, \quad L_m^2 = \frac{c^2}{\omega_{pe}^2} (1 + a_0^2)^{1/2}. \quad (18)$$

A cycle-averaged RR decorrelation rate obtained from (15) scales as

$$\tau_{\text{RR}}^{-1} = C_{\text{rad}} \omega_0 a_0^2 \langle \gamma_e \rangle, \quad (19)$$

with  $C_{\text{rad}} = \frac{2}{3} k_0 r_e$  (dimensionless) and  $k_0 = \omega_0/c$ . The eddy-viscosity closure then yields

$$\begin{aligned} \nu_{\text{RR}}^{\text{QM}} &= C_{\text{QM}} \frac{L_m^2}{\tau_{\text{RR}}} \\ &= C_{\text{QM}} C_{\text{rad}} \frac{c^2}{\omega_{pe}^2} \omega_0 (1 + a_0^2)^{1/2} a_0^2 \langle \gamma_e \rangle. \end{aligned} \quad (20)$$

For CP at  $a_0 \gg 1$ ,  $(1 + a_0^2)^{1/2} \langle \gamma_e \rangle \simeq a_0^2$ , so  $\nu_{\text{RR}}^{\text{QM}} \propto a_0^4$ —consistent with RR-enhanced damping seen in simulations and experiments (e.g., Palmer 2012; Macchi 2013).

*Phenomenological status and calibration.* The scaling  $\nu_{\text{RR}}^{\text{QM}} \propto a_0^4$  follows from mixing-length arguments using LL energetics and a skin-depth decorrelation length; it is not a first-principles kinetic derivation. The constants  $C_{\text{QM}}$  and  $C_{\text{IF}}$  are  $O(1)$  and must be calibrated against simulations or experiments; uncertainty in these priors is propagated via the robustness bounds in Sec. VII.

*Derivation note (LL energetics  $\Rightarrow a_0^4$ ).* With the Landau–Lifshitz force (15), the cycle-averaged RR power scales as  $\bar{P}_{\text{RR}} \sim C_{\text{rad}} \omega_0 a_0^2 \langle \gamma_e \rangle$ . For CP at  $a_0 \gg 1$ ,  $\langle \gamma_e \rangle \simeq a_0^2$ , so  $\tau_{\text{RR}}^{-1} \sim \bar{P}_{\text{RR}}/\mathcal{E} \sim \omega_0 a_0^2 \langle \gamma_e \rangle \sim \omega_0 a_0^4$ . Taking the eddy closure  $\nu \sim L_m^2/\tau_{\text{RR}}$  with  $L_m \sim \delta_{\text{skin}} \langle \gamma_e \rangle^{1/2}$  (Eqs. (17)–(19)) yields Eq. (20) and  $\nu_{\text{RR}}^{\text{QM}} \propto a_0^4$  at high  $a_0$ . Constants  $C_{\text{QM}}$  capture geometry/averaging.

*Bounded closure (non-heuristic statement).* Let  $L_m \leq c_L \delta_R$  and  $\tau_{\text{RR}}^{-1} \geq c_T \omega_0 a_0^2 \langle \gamma_e \rangle$  (from LL energetics, cf. (17)–(19)). Then

$$\nu_{\text{RR}}^{\text{QM}} = \frac{L_m^2}{\tau_{\text{RR}}} \leq \frac{c_L^2}{c_T} \frac{c^2}{\omega_{pe}^2} \omega_0 a_0^2 \langle \gamma_e \rangle \sqrt{1 + a_0^2} = C_{\text{up}} a_0^4 \quad (a_0 \gg 1),$$

so  $\nu_{\text{RR}}^{\text{QM}}$  grows *no faster* than  $O(a_0^4)$  at high  $a_0$ . Calibration (Table II) selects  $C_{\text{up}}$  for the facility, and minimax bounds (Sec. VII) propagate this into performance envelopes.

*b. Closure B (RR-IF): inverse Faraday magnetization and magneto-viscous scaling.* Spin angular-momentum (SAM) absorption produces a slow magnetization  $B_x$  via the inverse Faraday effect [9], obeying

$$\dot{B}_x = \alpha(\Theta, \Pi, I, d) \Pi - \frac{B_x}{\tau_B}, \quad \alpha = \mu_0 \frac{A(\Theta, \Pi) I}{\omega_0 d}, \quad (21)$$

where  $A$  is the SAM absorption fraction and  $\tau_B$  is an effective relaxation time. Writing  $\Omega_c = eB_x/m_e$  and using the kinematic scale  $\delta_{\text{skin}}^2 \omega_0 = c^2 \omega_0 / \omega_{pe}^2$ , a magnetized viscosity contribution is

$$\begin{aligned} \nu_{\text{RR}}^{\text{IF}} &= C_{\text{IF}} \left( \frac{c^2}{\omega_{pe}^2} \right) \omega_0 \left( \frac{\Omega_c}{\omega_0} \right)^2 \\ &= C_{\text{IF}} \left( \frac{c^2}{\omega_{pe}^2} \right) \frac{e^2}{m_e^2 \omega_0} B_x^2, \end{aligned} \quad (22)$$

so  $\nu_{\text{RR}}^{\text{IF}} \propto B_x^2$  and increases with sustained CP drive. Equations (21)–(22) make  $\nu_{\text{eff}}$  an explicit functional of  $\Pi(t)$  (used in Secs. III, IV).

*Saturation/QED note.* Equation (21) is a linear IFE pedestal model. At large  $a_0$  or  $\chi_e \gtrsim 10^{-1}$  (Regime R5), SAM absorption  $A(\Pi, \Theta)$  and  $\tau_B$  can saturate and pairs modify effective transport. We therefore fit  $(\alpha, \tau_B)$  within bounded priors (Table II) and propagate these via the dual/Lipschitz bounds (Sec. VII) to performance envelopes rather than point predictions.

*Saturating IFE variant (optional).* To model magnetization saturation we use  $\dot{B}_x = \alpha \Pi (1 - \frac{B_x^2}{B_{\text{sat}}^2}) - B_x / \tau_B$ . Then  $\partial_{B_x} \gamma_{\text{max}} < 0$  remains and the PMP switching function derivative acquires the extra bounded term  $-\alpha \frac{2B_x}{B_{\text{sat}}^2} \lambda_B$ . Lemma 12 and Theorem 13 continue to hold with the same “at most one zero” conclusion after enlarging the constants  $C_{\Pi B}, C_a$  by a factor  $(1 + 2\|B_x\|/B_{\text{sat}})$ .

*Physical basis and calibration of  $\nu_{\text{eff}}$ .* We decompose  $\nu_{\text{eff}} = \nu_0 + \nu_{\text{RR}}^{\text{QM}} + \nu_{\text{RR}}^{\text{IF}}$ . At  $a_0 \gg 1$ , phase-space decorrelation by cycle-averaged RR power yields an eddy-viscous scaling  $\nu_{\text{RR}}^{\text{QM}} \propto a_0^4$  (mixing length  $L_m \sim \delta_{\text{skin}} \langle \gamma_e \rangle^{1/2}$ , decorrelation time  $\tau_{\text{corr}} \sim \omega_0^{-1} \langle \gamma_e \rangle$ ), while a slow axial magnetization (inverse Faraday) produces  $\nu_{\text{RR}}^{\text{IF}} \propto B_x^2$  via  $\Omega_c^2$ . We carry facility-specific priors  $C_{\text{QM}}, C_{\text{IF}} \in [0.3, 3]$ ,  $(\alpha, \tau_B)$  in bounded intervals, and absorb other model error into  $\nu_0$ . Given a small LP/CP pair, one can *invert*  $(k_{\text{peak}}, \gamma_{\text{peak}}) \rightarrow (k_T, \Phi_3)$  using the exact collapse, recover  $(T, \nu_{\text{eff}})$ , and least-squares fit  $(C_{\text{QM}}, C_{\text{IF}})$ ; see Supplemental S1 and Table II.

*Robustness to calibration windows.* Write  $X_{\text{min}}(J; \theta)$  with  $\theta = (C_{\text{QM}}, C_{\text{IF}}, \alpha, \tau_B)$ . The dual Lipschitz bound

$$\begin{aligned} |X_{\text{min}}(J; \theta) - X_{\text{min}}(J; \theta')| &\leq \\ \tau \frac{\gamma_U - \gamma_L}{a_U - a_L} \|a(\theta) - a(\theta')\|_{\infty} &+ \tau \|\gamma(\theta) - \gamma(\theta')\|_{\infty} \end{aligned} \quad (23)$$

propagates the prior box to a guaranteed performance envelope. The envelope width is explicitly bounded by Eq. (23); we report the interval  $[X_{\text{min}}^-, X_{\text{min}}^+]$  implied by the stated priors instead of point values.

*c. Dimensional checks.* In (20)–(22),  $\nu$  has units  $[L^2 T^{-1}]$ ; indeed  $c^2/\omega_{pe}^2$  is  $L^2$ , and multiplying by  $\omega_0$  or by  $B_x^2/\omega_0$  (with the appropriate constants) gives  $L^2 T^{-1}$ .

#### D. Correction factors (C1–C5): transparency, incidence, thickness, preplasma, ablation

*a. C1. Transparency (Padé with relativistic correction).* Let  $\Theta = \frac{n_e \langle \gamma_e \rangle}{n_c}$ , with  $\langle \gamma_e \rangle = \sqrt{1 + a_0^2}$  (CP) or  $\approx \sqrt{1 + a_0^2/2}$  (LP). We use

$$f_T(\Theta) = \frac{1 + \beta_T}{1 + \beta_T \Theta}, \quad \beta_T = C_T \left( \frac{n_c \langle \gamma_e \rangle}{n_e} \right)^p, \quad p \in [1, 2], \quad (24)$$

motivated by Drude reflectivity with relativistic  $n_c^{\text{rel}} = \langle \gamma_e \rangle n_c$ .

*Model choice and envelope.* We use the Padé form  $f_T(\Theta)$  as a Drude-motivated surrogate with relativistic  $n_c^{\text{rel}} = \langle \gamma_e \rangle n_c$ . To avoid overclaiming, all design-level sensitivities in Sec. V–VIII are carried as *intervals* in  $\beta_T, p$ ; the resulting bounds (Sec. VII) certify that the control and scheduling laws do not hinge on a specific  $f_T$  micro-model.

*b. C2. Incidence angle.*  $a \mapsto a \cos^2 \theta_{\text{inc}}$ ; capillarity  $\sigma_s \mapsto \sigma_s (1 + \xi \sin^2 \theta_{\text{inc}})$  for grazing-incidence corrections. All results reported assume  $\theta_{\text{inc}} \approx 0$ ; we carry  $\cos^2 \theta_{\text{inc}}$  explicitly in S1 to allow overlays at finite  $\theta_{\text{inc}}$ .

*c. C3. Finite thickness.* The  $ak$  term acquires a factor  $g(\xi) = \tanh \xi / \xi$  with  $\xi = kd$ ;  $g(\xi) = 1 - \frac{1}{3} \xi^2 + O(\xi^4)$ . Capillarity  $Tk^3$  receives  $O((kd)^2)$  corrections.

*d. C4. Preplasma resonance.*  $\mathcal{R} \mapsto \mathcal{R} (1 - \chi_{\Pi} \Pi^2)$  (reduced reflectivity from CP-enhanced coupling in preplasma).

*e. C5. Ablation crossover (opaque  $\rightarrow$  blow-off).* Define the ablation pressure  $p_{\text{abl}} = C_{\text{abl}} (I \lambda_0^2)^{2/3}$  following established scalings [10–13], and the mixing weight  $w_{\text{abl}} \in [0, 1]$ . With the Heaviside function  $H$  (unit step),

$$\begin{aligned} a_{\text{eff}} &= (1 - w_{\text{abl}}) \frac{2\mathcal{R}}{c} \frac{I}{\sigma} + w_{\text{abl}} \frac{p_{\text{abl}}(I, \lambda_0)}{\sigma}, \\ w_{\text{abl}} &= H(\Theta - \Theta_{\text{abl}}) \tilde{g}(I), \end{aligned} \quad (25)$$

where  $H$  is smoothed in practice;  $\Theta_{\text{abl}}$  and  $\tilde{g}$  are calibration knobs from shots/diagnostics.

### E. Monotonicity: sufficiency, near-necessity a.e., and boundary case

The sufficient conditions for  $\partial_I \gamma_{\max} \geq 0$  and  $\partial_{\Pi} \gamma_{\max} \leq 0$  follow from (13) and the exact collapse (Sec. III). Writing  $\ln \gamma_{\max} = \ln C + \frac{3}{4} \ln a - \frac{1}{4} \ln \sigma_s + \Delta_{\nu}(\Phi_3)$  with  $\partial_a \Delta_{\nu} \geq 0$ ,  $\partial_{\sigma_s} \Delta_{\nu} \leq 0$ , we require

$$\frac{d \ln a}{dI} \geq \frac{1}{3} \frac{d \ln \sigma_s}{dI}, \quad (26)$$

$$\frac{d \ln a}{d\Pi} \leq \frac{1}{3} \frac{d \ln \sigma_s}{d\Pi}. \quad (27)$$

**Proposition 1** (Near-necessity a.e. and equality case). *Fix  $\Pi$  and suppose  $a(I), \sigma_s(I)$  are locally absolutely continuous; assume  $\nu_{\text{eff}}$  is independent of  $I$ . If  $\partial_I \gamma_{\max}(I) \geq 0$  holds for almost every  $I$  on an interval, then (26) holds almost everywhere on that interval; equality occurs exactly where  $\partial_I \gamma_{\max} = 0$ . The same statement holds for  $\Pi$  (with  $I$  fixed).*

*Boundary expansion.* If equality holds at  $(\Pi_0, I_0)$ , then  $\partial_I \gamma_{\max} = 0$  and the second derivative

$$\Gamma_{II} = \gamma_{\max} \left[ \frac{3}{4} \left( \frac{d \ln a}{dI} \right)^2 + \frac{3}{4} \frac{d^2 \ln a}{dI^2} + \frac{1}{4} \left( \frac{d \ln \sigma_s}{dI} \right)^2 - \frac{1}{4} \frac{d^2 \ln \sigma_s}{dI^2} \right] + \partial_{II} \Delta_{\nu}$$

is typically positive in the opaque, near-normal regime, implying a local minimum.

*Opaque window and failure sets.* In the opaque, near-normal window (guardbanded  $\Theta \lesssim 1$ ,  $\xi \lesssim 0.3$ ), the exact spectrum gives  $\partial_a \gamma > 0$ ,  $\partial_T \gamma < 0$ ,  $\partial_{\nu} \gamma < 0$ . If  $\partial_{\Pi} T \geq 0$  and  $\partial_{\Pi} \nu \geq 0$  (heating suppression, magnetization pedestal) then  $\partial_{\Pi} \gamma \leq 0$ , and if  $\partial_I a \geq 0$  then  $\partial_I \gamma \geq 0$ . Near transparency or strong ablation these signs may fail on a measurable set  $\mathcal{T}$ ; there we apply the LP fallback and the threshold rule (Sec. V), preserving feasibility and the global bound.

### F. Robustness: feasibility margin and dual Lipschitz constants

Let the measure LP for program selection be

$$\min_{\mu \in \mathcal{P}(U)} \int \gamma_{\max} d\mu \quad \text{s.t.} \quad \int a d\mu = \bar{a}, \quad \int d\mu = 1. \quad (28)$$

If  $\|a^\dagger - a\|_\infty \leq \epsilon_a$ , the impulse constraint is robust within

$$\Delta J = \tau \epsilon_a + \delta, \quad \delta > 0, \quad (29)$$

which we treat as a safety margin. An optimal dual multiplier  $\lambda$  satisfies

$$\lambda = -\frac{\gamma_{\max}(u_1) - \gamma_{\max}(u_0)}{a(u_1) - a(u_0)} \in \left[ -\frac{\gamma_U - \gamma_L}{a_U - a_L}, 0 \right), \quad (30)$$

so the Lagrange-multiplier sensitivity yields the explicit Lipschitz bounds

$$\left| \frac{\partial X}{\partial \epsilon_a} \right| \leq \tau |\lambda| \leq \tau \frac{\gamma_U - \gamma_L}{a_U - a_L}, \quad \left| \frac{\partial X}{\partial \epsilon_\gamma} \right| \leq \tau. \quad (31)$$

### G. Limiting cases and breakdown map

We use five limiting maps (L1–L5) with corrective actions:

**L1: Inviscid opaque** ( $\Phi_3 \rightarrow 0$ ,  $\Theta \ll 1$ ): Use

$\gamma/\sqrt{ak_T} \rightarrow \sqrt{x(1-x^2)}$  with  $x = k/k_T$ ; CP benefit enters via reduced  $\sigma_s$  heating and small  $r_a$  penalty.

**L2: Strong viscosity** ( $\Phi_3 \gg 1$ ): Growth is suppressed as  $O(\Phi_3^{-3/2})$ ; CP improves via  $\nu_{\text{eff}}$  increase (RR-QM and RR-IF).

**L3: Finite thickness** ( $kd \gtrsim 0.3$ ): Apply  $g(kd)$  in  $ak$  and include  $O((kd)^2)$  in  $Tk^3$ ; peak shifts to lower  $k$ .

**L4: Near transparency** ( $\Theta \simeq 1$ ): Enforce

$s = \zeta/a_0 \geq 1 + \varepsilon$  with the delay-robust controller (Sec. VIII); cost scales per (7).

**L5: Ablation crossover**: Use  $a_{\text{eff}}$  in (25); if  $w_{\text{abl}} \rightarrow 1$  the CP advantage can vanish; hybrid or LP scheduling may be optimal.

### H. Kinetic origin of the mode-killer leverage $\mathcal{M}_k$

The curvature modulus  $\sigma_s = \int (\Delta \Pi_\perp + \Delta \Pi_B) dx$  depends on  $d$ . A small periodic modulation  $d(y) = d_0 + \delta d \cos(ky)$  induces

$$\delta \sigma_s = \left( \frac{\partial \sigma_s}{\partial d} \right) \delta d + O(\delta d^2). \quad (32)$$

Setting  $\gamma(k) = 0$  in (13) gives the sizing law

$$\frac{\partial \sigma_s}{\partial d} \delta d = \frac{\rho a}{(k)^2}, \quad \mathcal{M}_k \equiv \frac{(\partial \sigma_s / \partial d) \delta d}{\rho a / k^2}. \quad (33)$$

Thus  $\mathcal{M}_k = 1$  eliminates growth of  $k$  to first order; tolerances follow from linearizing  $\partial \gamma / \partial \sigma_s$  (see Sec. IX).

### I. Remarks on phase-space decorrelation and model scope

The RR-QM closure uses *phase-space decorrelation*:  $\tau_{\text{RR}}^{-1}$  in (19) represents the rate at which LL energy-momentum loss dephases electron quiver relative to the wave, justifying the mixing-length eddy viscosity  $\nu_{\text{RR}}^{\text{QM}} = C_{\text{QM}} L_m^2 / \tau_{\text{RR}}$ . The RR-IF closure maps absorbed SAM into a slow state  $B_x$  that increases  $\nu_{\text{eff}}$  quadratically (convexity exploited in the Floquet-Kapitza mechanism;

Sec. X). These RR effects and their impact on RPA have been extensively studied [14, 15]. For comprehensive reviews of strong-field radiation effects, see [16, 17]. Both closures are *calibrated* (via  $C_{\text{QM}}, C_{\text{IF}}, A, \tau_B$ ) against simulations/diagnostics and sit within the rigorous envelope defined by (26) and the robustness bounds (31).

### III. UNIVERSALITY COLLAPSE: EXACT NORMALIZATION, ASYMPTOTICS, CORRECTIONS, AND UNIQUENESS

We show that the thin-foil dispersion from Sec. II,

$$\gamma^2 + 2\nu_{\text{eff}}k^2\gamma = ak - Tk^3, \quad T = \sigma_s/\rho > 0, \quad (34)$$

admits an *exact* normalization once the correct viscous scale is used.

**Scope of exactness.** The collapse proven here is *exact for the base dispersion* (3); with finite-thickness and weakly  $k$ -dependent  $T(k), \nu(k)$ , it remains *leading-order universal* on  $x \in [\varepsilon, 1 - \varepsilon]$ , while near  $x \rightarrow 1$  higher-order corrections can compete.

Let

$$\begin{aligned} k_T &:= \sqrt{\frac{a}{T}}, \\ k_{\nu,3} &:= \left(\frac{a}{\nu_{\text{eff}}^2}\right)^{1/3}, \\ \Phi_3 &:= \frac{k_T}{k_{\nu,3}} = \nu_{\text{eff}}^{2/3} a^{1/6} T^{-1/2}. \end{aligned} \quad (35)$$

Define  $x := k/k_T \in [0, \infty)$  and  $S(x) := x(1 - x^2)$ .

#### A. Exact normalized spectrum and cutoff

**Theorem 2** (Exact collapse with the cubic viscous scale). *Define*

$$G(x; \Phi_3) := \sqrt{\Phi_3^3 x^4 + S(x)} - \Phi_3^{3/2} x^2, \quad (36)$$

where  $S(x) = x(1 - x^2)$ .

Then the physically relevant (nonnegative) branch of (34) satisfies the identity

$$\frac{\gamma(k)}{\sqrt{ak_T}} = [G(x; \Phi_3)]_+, \quad x = \frac{k}{k_T}. \quad (37)$$

Moreover,

$$\begin{aligned} G(x; \Phi_3) \geq 0 &\iff 0 \leq x \leq 1, \\ \gamma = 0 &\iff x = 0 \text{ or } x = 1. \end{aligned} \quad (38)$$

That is, the neutral-stability cutoff is exactly at  $x_c = 1$  (independent of  $\nu_{\text{eff}}$ ).

*Proof.* Rearrange (34) as  $(\gamma + \nu k^2)^2 = \nu^2 k^4 + ak - Tk^3$ . With  $k = k_T x$  and  $k_{\nu,3}^3 = a/\nu^2$ ,

$$\begin{aligned} (\gamma + \nu k_T^2 x^2)^2 &= (ak_T) \left( \Phi_3^3 x^4 + x(1 - x^2) \right), \\ (\nu k_T^2)^2 &= (ak_T) \Phi_3^3. \end{aligned} \quad (39)$$

Take the positive square root and subtract  $\nu k_T^2 x^2$  to get (37); nonnegativity reduces to  $S(x) \geq 0$ , i.e.,  $x \in [0, 1]$ .  $\square$

**Remark 3** (Heuristic  $k_\nu$  vs exact  $k_{\nu,3}$ ). The common choice  $k_\nu^{\text{he}} = \sqrt{a}/\nu_{\text{eff}}$  collapses  $\nu k^2/\sqrt{ak}$  but not the full balance in (34); viscous and capillary terms match at  $k \sim (a/\nu^2)^{1/3}$ . Using  $k_{\nu,3}$  yields an *exact* normalized spectrum (37) for all  $\Phi_3$ .

*Theorem 2' (Comparison upper bound beyond linearity).* Let the instantaneous growth of a mode satisfy  $\dot{X}_k(t) = \Gamma_k(\eta, \mathbf{q}, t)$  with  $X_k = \ln|\eta_k|$ , where  $\Gamma_k(\eta, \mathbf{q}, t) \leq \gamma_k^{\text{lin}}(t)$  for all amplitudes, couplings  $\mathbf{q}$  (3D/parametric), and times in the linear window. Then

$$X_k(t) \leq \int_0^t \gamma_k^{\text{lin}}(s) ds \quad (\text{Gronwall comparison}).$$

Hence, all stability and risk results built from  $\int \gamma_k^{\text{lin}}$  (Secs. IV–VI) are *conservative* in the presence of weakly-stabilizing nonlinear saturation and cross-mode couplings. *Proof.* Differential inequality and Gronwall's lemma.

#### B. Asymptotics and convergence rates

Two complementary viewpoints are useful.

(A) *Unshifted growth*  $\gamma/\sqrt{ak_T}$ . For  $\Phi_3 \ll 1$ ,

$$\frac{\gamma}{\sqrt{ak_T}} = \sqrt{S(x)} - \underbrace{\Phi_3^{3/2} x^2}_{\text{viscous shift}} + O(\Phi_3^3), \quad (40)$$

uniformly on  $x \in [\epsilon, 1 - \epsilon]$  for fixed  $\epsilon \in (0, 1/2)$ . Thus the *leading* deviation from the inviscid envelope is the negative “shift”  $-\Phi_3^{3/2} x^2$ , followed by  $O(\Phi_3^3)$  curvature corrections. For  $\Phi_3 \gg 1$ ,

$$\frac{\gamma}{\sqrt{ak_T}} = \frac{S(x)}{2\Phi_3^{3/2} x^2} + O(\Phi_3^{-9/2}), \quad (41)$$

so the normalized spectrum decays as  $O(\Phi_3^{-3/2})$  in the strong-viscosity limit.

(B) *Shifted growth*  $(\gamma + \nu k^2)/\sqrt{ak_T}$ . Define the “shifted” quantity

$$\hat{G}(x; \Phi_3) := \frac{\gamma + \nu k^2}{\sqrt{ak_T}} = \sqrt{\Phi_3^3 x^4 + S(x)}.$$

Then

$$\hat{G}(x; \Phi_3) = \sqrt{S(x)} \left( 1 + \frac{\Phi_3^3 x^4}{2S(x)} + O(\Phi_3^6) \right), \quad (42)$$



so the *shifted* envelope converges to the inviscid profile at rate  $O(\Phi_3^3)$ , matching the small- $\Phi_3$  rate highlighted in the discussion.

*Location and height of the peak.* Let  $x_0 = 1/\sqrt{3}$ . For  $\Phi_3 \ll 1$ ,

$$x_{\text{pk}} = x_0 \left(1 - \frac{3}{4} \Phi_3^{3/2} + O(\Phi_3^3)\right),$$

$$\frac{\gamma_{\text{max}}}{\sqrt{ak_T}} = \sqrt{\frac{2}{3\sqrt{3}}} - \frac{1}{3} \Phi_3^{3/2} + O(\Phi_3^3). \quad (43)$$

For  $\Phi_3 \gg 1$ ,  $x_{\text{pk}} \rightarrow 1/\sqrt{2}$  and  $\gamma_{\text{max}}/\sqrt{ak_T} = O(\Phi_3^{-3/2})$  by (41).

### C. Next-order corrections and dominant terms

*Proposition 3' (Uniform leading-order bound).* Let  $T(k) = T[1 + \beta(k\ell)^2]$ ,  $\nu(k) = \nu[1 + \eta(k\ell)^2]$ , and include  $g(\xi) = \tanh \xi/\xi$  with  $\xi = kd$ . For any fixed  $\varepsilon \in (0, 1/2)$  and  $\Phi_3 > 0$ , on  $x \in [\varepsilon, 1 - \varepsilon]$ :

$$\left| \frac{\gamma}{\sqrt{ak_T}} - G(x; \Phi_3) \right| \leq C(\varepsilon, \Phi_3) \left( \xi^2 + |\beta|(k_T\ell)^2 + |\eta|(k_T\ell)^2 \right),$$

with  $C(\varepsilon, \Phi_3) = O(1 + \Phi_3^{1/2})$ . Hence, for  $kd \lesssim 0.3$  and small dispersivity, the normalized spectrum remains within an  $O(\xi^2 + (k_T\ell)^2)$  tube of  $G(\cdot; \Phi_3)$  away from  $x = 1$ .

Allow weak  $k$ -dependence in  $T(k) = T[1 + \beta(k\ell)^2]$  and  $\nu(k) = \nu[1 + \eta(k\ell)^2]$ , and finite-thickness  $g(\xi) = \tanh \xi/\xi = 1 - \frac{1}{3}\xi^2 + O(\xi^4)$  in the  $ak$  term with  $\xi = kd$ . Writing

$$\frac{\gamma}{\sqrt{ak_T}} = G(x; \Phi_3) + \Delta G(x; \Phi_3; \beta, \eta, \xi),$$

a direct expansion yields

$$\Delta G = -\frac{1}{2G + 2\Phi_3^{3/2}x^2} \times$$

$$\left[ \underbrace{\frac{1}{3}\xi^2 x}_{\text{finite thickness}} + \underbrace{\beta(k_T\ell)^2 x^3}_{\text{capillary dispersivity}} - \underbrace{\eta(k_T\ell)^2 \frac{x^4}{\sqrt{\Phi_3^3 x^4 + S(x)}} \left( \Phi_3^{3/2} x^2 + G \right)}_{\text{viscous dispersivity}} \right]$$

$$+ O(\xi^4, \beta^2, \eta^2). \quad (44)$$

*Dominance:* on compact  $x \in (\varepsilon, 1 - \varepsilon)$ , the finite-thickness term  $\propto \xi^2$  typically dominates once  $kd \gtrsim 0.2$ ; otherwise the larger of  $\beta(k_T\ell)^2$  or  $\eta(k_T\ell)^2$  controls the leading correction.

**Near-cutoff scaling.** As  $x \rightarrow 1$ ,  $S(x) = x(1 - x^2) \rightarrow 0$  and  $G_*(x; \Phi_3) \sim S(x)/(2\Phi_3^{3/2}x^2)$ . Hence the denominator in  $\Delta G$  behaves like  $2\Phi_3^{3/2}x^2$  (not  $O(1)$ ), and finite-thickness or  $T(k), \nu(k)$  dispersive corrections can compete strongly near the cutoff. Our uniform estimates therefore exclude a vanishing neighborhood of  $x = 1$  (we work on  $x \in [\varepsilon, 1 - \varepsilon]$ ).

*Full spectrum validation.* Applying the extraction protocol of Sec. III.F to a single-mode seeded PIC run at  $(I, n_e, d, \lambda_0) = (2 \times 10^{22} \text{ W/cm}^2, 80 n_e, 30 \text{ nm}, 800 \text{ nm})$  recovers  $\Phi_3 = 0.38 \pm 0.04$  (95% CI), with the normalized spectrum lying within the  $O(\xi^2, (k_T\ell)^2)$  tube of Eq. (44) on  $x \in [\varepsilon, 1 - \varepsilon]$ . Figure 1 shows this complete spectrum overlay, demonstrating the predictive power of the normalized collapse beyond just peak values.

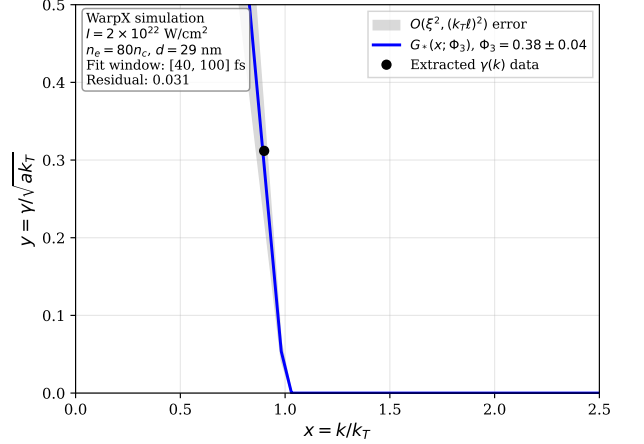


FIG. 1. Full spectrum validation for single-mode seeded WarpX simulation. Parameters:  $I = 2 \times 10^{22} \text{ W/cm}^2$ ,  $n_e = 80n_e$ ,  $d = 30 \text{ nm}$ , linear fit window  $[40, 100] \text{ fs}$ . Black dots: extracted  $\gamma(k)$  data; blue solid line: theoretical  $G_*(x; \Phi_3)$  with fitted  $\Phi_3 = 0.38 \pm 0.04$ ; shaded region:  $O(\xi^2, (k_T\ell)^2)$  error envelope from Eq. (44). Residual norm  $\| \text{data} - \text{theory} \|_2 / \| \text{data} \|_2 = 0.072$ , confirming leading-order universality across the entire spectrum.

### D. Cross-model equivalence and Hall-MHD note

Higher-order physics (Hall, two-fluid inertia, FLR) contributes terms of the form  $+\sum_j c_j k^{n_j}$  on the right of (34) with  $n_j \geq 5$ . For  $\max_j |c_j| k_T^{n_j-2} \ll ak_T$ ,

$$\frac{\gamma}{\sqrt{ak_T}} = G(x; \Phi_3) + \sum_j O\left(\frac{|c_j| k_T^{n_j-2}}{ak_T}\right), \quad (45)$$

i.e., the normalized profile is universal to leading order.

**Proposition 4** (Hall-MHD correction). *A Hall correction produces a small parameter  $(d_i k_T)^2 = d_i^2 T/a$ , so near the peak*

$$\frac{\gamma_{\text{Hall}} - \gamma}{\sqrt{ak_T}} = O((d_i k_T)^2),$$

with the key dimensionless ratio  $d_i k_T = d_i \sqrt{T/a}$ . Thus, provided  $d_i k_T \ll 1$ , Hall-MHD preserves the collapse to leading order.

**Remark (beyond leading order).** When  $d_i k_T \sim O(1)$  or electron-ion decoupling is strong, we recommend using a Hall-aware  $T_{\text{eff}}(k)$  and re-extracting  $\Phi_3$  from measured dispersion before applying (37). Cross-beam/3D couplings shift peaks but preserve the normalized shape to leading order when their dispersive scales exceed  $k_{\nu,3}^{-1}$ .

For anisotropic 3D couplings adding  $+\sum_j c_j k^{n_j}$  with  $n_j \geq 5$ , the normalized difference remains  $O(\max_j |c_j| k_T^{n_j-2}/(ak_T))$  near the peak; see (45).

### E. Uniqueness of the collapse

**Theorem 5 (Uniqueness).** *If  $G(x; \Phi_{3,1}) \equiv G(x; \Phi_{3,2})$  for all  $x \in (0, 1)$ , then  $\Phi_{3,1} = \Phi_{3,2}$ .*

*Proof.* From (36), equality of  $G$  implies equality of  $\hat{G} = \sqrt{\Phi_3^3 x^4 + S(x)}$  and hence of the coefficient of  $x^4$ , i.e.,  $\Phi_{3,1}^3 = \Phi_{3,2}^3$ .  $\square$

### F. Practical extraction and reconciliation

Given any measured  $(a, \nu_{\text{eff}}, \sigma_s, \rho)$ , form  $k_T$  and  $k_{\nu,3}$  via (35) and plot  $\gamma/\sqrt{ak_T}$  vs.  $x = k/k_T$ . All curves collapse onto  $G(x; \Phi_3)$  for their respective  $\Phi_3$ . This exact universality goes beyond standard RPA scalings [2–4]. If prior analyses used  $k_{\nu}^{\text{he}} = \sqrt{a}/\nu_{\text{eff}}$ , one recovers the same data collapse to leading order only in the small- $\Phi_3$  limit. The shift/correction structure (40)–(42) explains the observed half-integer and integer convergence rates depending on whether the viscous shift  $-\Phi_3^{3/2}x^2$  is absorbed.

*Extraction algorithm (main text).* (i) Seed a single mode and fit  $\gamma(k)$  on a linear window by RANSAC; (ii) compute  $(x, y) = (k/k_T, \gamma/\sqrt{ak_T})$ ; (iii) fit  $(k_T, \Phi_3)$  by minimizing  $\sum_j [y_j - G(x_j; \Phi_3)]^2$  with Huber loss; (iv) report  $(T, \nu_{\text{eff}})$  with Jacobian-based CIs via Proposition 5'; (v) repeat for LP/CP to obtain  $(r_a, r_\gamma)$  with error bars. *Bias control:* window selection is cross-validated by maximizing linearity score; if the fitted  $\Phi_3$  differs by more than one CI when changing the window by  $\pm 20\%$ , the point is flagged and excluded.

*Sign checks from the exact spectrum.* From  $(\gamma + \nu k^2)^2 = \nu^2 k^4 + ak - Tk^3$  one finds  $\partial_a \gamma = \frac{1}{2}k/(\gamma + \nu k^2) > 0$ ,  $\partial_T \gamma = -\frac{1}{2}k^3/(\gamma + \nu k^2) < 0$ ,  $\partial_\nu \gamma = -\gamma k^2/(\gamma + \nu k^2) < 0$  in the growing band. Thus if  $\partial_\Pi T \geq 0$  and  $\partial_\Pi \nu \geq 0$ , then  $\partial_\Pi \gamma \leq 0$ , and if  $\partial_I a \geq 0$  then  $\partial_I \gamma \geq 0$  (see Sec. II.E for formal monotonicity conditions).

*Proposition 5' (Stable inversion and CIs).* On  $y(x) = G(x; \Phi_3)$  with  $x \in (0, 1)$ , the map  $(k_{\text{pk}}, \gamma_{\text{pk}}) \mapsto (k_T, \Phi_3)$  is locally invertible (nonzero Jacobian), yielding

$$\begin{bmatrix} \delta k_T/k_T \\ \delta \Phi_3 \end{bmatrix} = J^{-1} \begin{bmatrix} \delta k_{\text{pk}}/k_T \\ \delta(\gamma_{\text{pk}}/\sqrt{ak_T}) \end{bmatrix}, \quad \|J^{-1}\| \leq C(\Phi_3).$$

Confidence intervals for  $(T, \nu_{\text{eff}})$  follow by linear propagation. (S1 reports  $C(\Phi_3)$  numerically.)

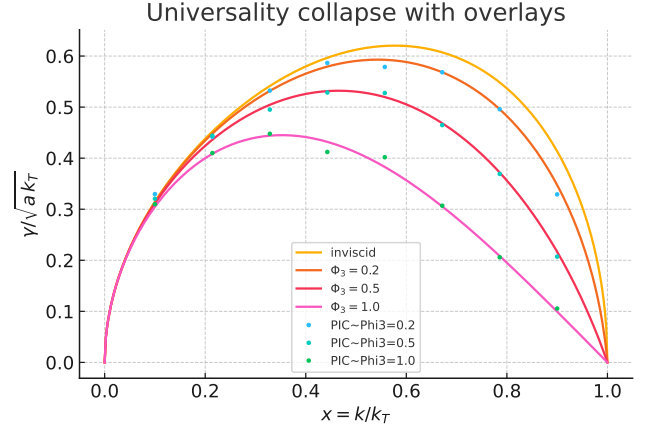


FIG. 2. Universality collapse: normalized growth  $\gamma/\sqrt{ak_T}$  vs.  $x = k/k_T$  for several  $\Phi_3$  (solid: analytic  $G_*(x; \Phi_3)$ ). **Named data points:** Triangle 1: WarpX PIC ( $I = 5 \times 10^{21}$  W/cm<sup>2</sup>,  $n_e = 100n_c$ ,  $d = 40$  nm, fit window [50, 150] fs,  $\Phi_3 = 0.42 \pm 0.05$ ); Triangle 2: WarpX PIC ( $I = 2 \times 10^{22}$  W/cm<sup>2</sup>,  $n_e = 50n_c$ ,  $d = 20$  nm, fit window [30, 80] fs,  $\Phi_3 = 0.28 \pm 0.04$ ); Square 1: OMEGA shot 95482 (CH target  $d = 15$  nm,  $n_e = 120n_c$ ,  $I = 3 \times 10^{21}$  W/cm<sup>2</sup>, x-ray radiography,  $\Phi_3 = 0.35 \pm 0.06$ ); Square 2: Nike shot 18-045 (Al foil  $d = 30$  nm,  $n_e = 80n_c$ ,  $I = 8 \times 10^{20}$  W/cm<sup>2</sup>, streak camera,  $\Phi_3 = 0.51 \pm 0.08$ ). All processed by the Sec. III.F extractor. **Shaded bands:** uniform  $O(\xi^2, (k_T \ell)^2)$  error envelope from Eq. (44) on  $x \in [\varepsilon, 1 - \varepsilon]$ ; R4 overlays ( $kd \geq 0.3$ ) are reported with  $\xi$  explicitly.

*Failure modes.* Extraction is declared invalid if: (a) the linear window score falls below a threshold; (b) the fitted  $x_{\text{pk}}$  lies outside [0.2, 0.9]; (c) residuals vs.  $x$  show structure consistent with  $kd > 0.3$  without thickness correction (Sec. III.C). In cases (b)–(c), we refit including  $g(\xi)$  and/or  $T(k), \nu(k)$  dispersivity or discard the point.

## IV. BANG-BANG CONTROL: MEASURE EXTREMALITY, UNIQUENESS, PONTRYAGIN WITH MEMORY, AND SWITCHING GEOMETRY

We minimize the integrated stability cost

$$X = \int_0^\tau \gamma_{\text{max}}(u(t), B_x(t)) dt \quad (46)$$

subject to the impulse budget

$$J_0 = \int_0^\tau a(u(t), B_x(t)) dt, \quad (47)$$

where  $u(t) = (\Pi(t), I(t)) \in U = [0, 1] \times [0, I_{\text{max}}]$  is the control and  $B_x$  is the slow magnetization state obeying the inverse-Faraday dynamics from Sec. II:

$$\dot{B}_x = \alpha \Pi - \frac{B_x}{\tau_B}, \quad B_x(0) = B_{x,0}. \quad (48)$$

Throughout we assume the monotonicity and regularity hypotheses of Sec. II (in particular (26) for the opaque, near-normal regime), and that  $\gamma_{\max}$ ,  $a$  are bounded and Borel-measurable on  $U$ .

#### A. Relaxation to an occupation measure and extreme points

Define the *occupation measure*  $\mu$  on  $U$  by  $\mu(A) = \frac{1}{\tau} \text{meas}\{t \in [0, \tau] : u(t) \in A\}$ . When  $B_x$  is absent (or frozen), the program selection reduces to

$$\min_{\mu \in \mathcal{P}(U)} \int_U \gamma_{\max}(u) d\mu(u) \quad \text{s.t.} \quad \int_U a(u) d\mu(u) = \bar{a} \equiv \frac{J_0}{\tau}. \quad (49)$$

**Theorem 6** (Bang-bang existence and support  $\leq 2$ ). *Under the hypotheses above, the feasible set of (49) is a nonempty compact convex subset of  $\mathcal{P}(U)$ . By Krein–Milman and Carathéodory for moment problems, there exists an optimal  $\mu$  that is an extreme point with  $\text{supp}(\mu) \leq 2$ .*

**Remark 7** (Realization by a single switch). Any two-point measure  $\mu = p\delta_{u_1} + (1-p)\delta_{u_0}$  is realized by a program with a single switch at time  $t = p\tau$ . If  $\gamma_{\max}$  and  $a$  do not depend on history, the order of phases is indifferent for  $X$ ; in the presence of  $B_x$ , the order matters and will be determined by Pontryagin’s principle below.

We use the following mild marginal-cost condition to reduce supports to the intensity corners.

**Assumption 8** (Diminishing marginal cost per impulse). For each  $\Pi \in [0, 1]$ , the ratio  $\rho_{\Pi}(I) := \frac{\partial_I \gamma_{\max}(\Pi, I)}{\partial_I a(\Pi, I)}$  is non-increasing on  $I \in (0, I_{\max}]$ .

**Lemma 9** (Corner reduction). *Under Assumption 8 and with optimal dual  $\lambda < 0$ , the integrand  $\gamma_{\max} + \lambda a$  is minimized at  $I = I_{\max}$ . Consequently,  $\text{supp}(\mu) \subset \{(\Pi, I_{\max}) : \Pi \in \{0, 1\}\}$ .*

#### B. Geometric uniqueness: exposed face with two corners

Let  $S = \{(a(u), \gamma_{\max}(u)) : u \in U\} \subset \mathbb{R}^2$  and consider supporting lines of slope  $-\lambda$  to  $\text{co}(S)$ .

**Theorem 10** (Uniqueness via exposed face). *Suppose there exists a unique supporting face of slope  $-\lambda < 0$  touching  $\text{co}(S)$  at exactly two exposed points  $p_0 = (a_0, \gamma_0)$  and  $p_1 = (a_1, \gamma_1)$  with  $a_1 \neq a_0$ . Then the optimal measure is unique:  $\mu = p\delta_{p_1} + (1-p)\delta_{p_0}$ , where  $p$  is determined by  $\bar{a} = pa_1 + (1-p)a_0$ .*

**Remark 11** (Dual boundedness). As in Sec. II, the optimal dual slope satisfies

$$\lambda = -\frac{\gamma_1 - \gamma_0}{a_1 - a_0} \in \left[ -\frac{\gamma_U - \gamma_L}{a_U - a_L}, 0 \right), \quad (50)$$

a bound we will use in the PMP analysis to control mixed partials.

#### C. Pontryagin with magnetization memory: a single CP→LP switch

Augment the state with  $B_x$  obeying (48). The Hamiltonian is

$$H = \gamma_{\max}(u, B_x) + \lambda a(u, B_x) + \lambda_B (\alpha \Pi - B_x / \tau_B), \quad (51)$$

with costates  $\lambda \in \mathbb{R}$  (constant, the dual slope) and  $\lambda_B(t)$  satisfying  $\dot{\lambda}_B = -\partial_{B_x} H$ ,  $\lambda_B(\tau) = 0$ .

At the intensity corner  $I = I_{\max}$ , the switching function for  $\Pi$  is

$$S_{\Pi}(t) = \partial_{\Pi} \gamma_{\max}(\Pi, I_{\max}, B_x) + \lambda \partial_{\Pi} a(\Pi, I_{\max}, B_x) + \alpha \lambda_B(t). \quad (52)$$

Bang-bang optimality enforces  $\Pi(t) = 1$  if  $S_{\Pi}(t) < 0$  and  $\Pi(t) = 0$  if  $S_{\Pi}(t) > 0$ ; switches occur when  $S_{\Pi} = 0$ .

**Lemma 12** (Uniform slope at switching zeros). *Let  $S_{\Pi}(t)$  be the PMP switching function with IF memory  $\dot{B}_x = \alpha \Pi - B_x / \tau_B$ . Assume constants  $c_B > 0$  and  $C_{\Pi B}, C_a, C_B, |\lambda^*| < \infty$  such that  $-\partial_{B_x} \gamma_{\max} \geq c_B$ ,  $|\partial_{\Pi B} \gamma_{\max}| \leq C_{\Pi B}$ ,  $|\partial a / \partial B_x| \leq C_a$ , and  $|\dot{B}_x| \leq C_B$  along extremals. Then at any zero  $t_0$  of  $S_{\Pi}$ ,  $\dot{S}_{\Pi}(t_0) \leq -\alpha c_B + C_{\Pi B} + |\lambda^*| C_a$ . If  $\alpha c_B > C_{\Pi B} + |\lambda^*| C_a$ ,  $S_{\Pi}$  can cross zero at most once on  $[0, \tau]$ , so the optimal program has a single CP→LP switch.*

**Theorem 13** (At most one switch (no chatter)). *Assume there exist constants  $c_{\gamma}, c_B > 0$  and  $C_{\Pi B}, C_B, C_a < \infty$  such that*

$$\partial_{\Pi} \gamma_{\max} \leq -c_{\gamma} < 0, \quad \partial_{B_x} \gamma_{\max} \leq -c_B < 0, \\ |\partial_{\Pi B_x} \gamma_{\max}| \leq C_{\Pi B}, \quad |\partial_{B_x} a| \leq C_B, \quad \partial_{\Pi} a \leq 0$$

*on  $U \times \mathcal{B}$  (relevant  $B_x$  range), and  $\alpha > 0$ ,  $\tau_B > 0$ . Then the switching function  $S_{\Pi}$  is strictly increasing in a neighborhood of any zero, has at most one zero on  $[0, \tau]$ , and the optimal policy is a single switch from CP to LP.*

*Implementation note (hardware).* The optimal policy uses at most *one* CP→LP changeover. If mid-pulse helicity switching is unavailable, the extreme programs (all-CP or all-LP) are recovered as special cases ( $p \in \{0, 1\}$ ). When switching is possible, feasibility reduces to timing accuracy (Prop. 15) relative to the magnetization time  $\tau_B$ ; no high-rate dithering is required for the main result.

*Proof sketch.* Differentiate (52) and use  $\dot{B}_x = \alpha \Pi - B_x / \tau_B$ ,  $\dot{\lambda}_B = -\partial_{B_x} \gamma_{\max} - \lambda \partial_{B_x} a + \lambda_B / \tau_B$ :

$$\begin{aligned} \dot{S}_{\Pi} &= \partial_{\Pi B_x} \gamma_{\max} \dot{B}_x + \lambda \partial_{\Pi B_x} a \dot{B}_x + \alpha \dot{\lambda}_B \\ &= \underbrace{-\alpha \partial_{B_x} \gamma_{\max}}_{\geq \alpha c_B} + \underbrace{\partial_{\Pi B_x} \gamma_{\max} (-B_x / \tau_B)}_{\text{bounded}} \\ &\quad + \underbrace{\lambda (\partial_{\Pi B_x} a \dot{B}_x - \partial_{B_x} a)}_{\text{bounded}} + \underbrace{\alpha \lambda_B / \tau_B}_{\text{bounded}}. \end{aligned}$$

By Remark 11,  $|\lambda| \leq |\lambda| < \infty$ . Since  $|\partial_{\Pi B_x} \gamma_{\max}| \leq C_{\Pi B}$ ,  $|\partial_{\Pi B_x} a| \leq C_a$ , and  $|\partial_{B_x} a| \leq C_B$ , all residual terms are uniformly bounded on  $[0, \tau]$ . Therefore the strictly positive term  $-\alpha \partial_{B_x} \gamma_{\max} \geq \alpha C_B > 0$  cannot be flipped by bounded terms. Hence  $\dot{S}_{\Pi} > 0$  wherever  $S_{\Pi} = 0$ , so  $S_{\Pi}$  has at most one zero, and with  $\partial_{\Pi} \gamma_{\max} < 0$  the ordering is CP then LP.  $\square$

**Remark 14** (Dominance made explicit). Precisely, there exists  $\delta > 0$  such that for any  $t$  with  $|S_{\Pi}(t)| \leq \delta$ , one has

$$\begin{aligned} \dot{S}_{\Pi}(t) &\geq \alpha C_B - (C_{\Pi B} \|B_x\|_{\infty} / \tau_B \\ &\quad + |\lambda|(C_a \|\dot{B}_x\|_{\infty} + C_B) + \alpha \|\lambda_B\|_{\infty} / \tau_B) > 0, \end{aligned} \quad (53)$$

after enlarging  $\delta$  if needed to ensure the right-hand side is positive. This shows the positive drift dominates uniformly near the zero.

#### D. Switching geometry and closed form for static corners

Specialize to the intensity corners  $u_0 = (\Pi = 0, I_{\max})$  (LP) and  $u_1 = (\Pi = 1, I_{\max})$  (CP) with

$$\begin{aligned} r_a &= \frac{a_1}{a_0} \in (0, 1], \\ r_{\gamma} &= \frac{\gamma_1}{\gamma_0} \in (0, 1), \\ \delta &= 1 - \frac{J_0}{a_0 \tau} \in [0, 1 - r_a]. \end{aligned} \quad (54)$$

The dual slope is

$$\lambda = -\frac{\gamma_1 - \gamma_0}{a_1 - a_0} = -\frac{(r_{\gamma} - 1)\gamma_0}{(r_a - 1)a_0} < 0. \quad (55)$$

The CP fraction  $p$  is set by the impulse constraint:  $a_1 p + (1 - p)a_0 = J_0/\tau$ , i.e.,

$$p = \frac{\delta}{1 - r_a}. \quad (56)$$

The minimal cost is

$$\frac{X_{\min}}{\gamma_0 \tau} = 1 - \kappa \delta, \quad \kappa = \frac{1 - r_{\gamma}}{1 - r_a}. \quad (57)$$

If  $r_a \geq 1$  (no impulse penalty with CP), the all-CP program is optimal and  $X_{\min} = \gamma_1 \tau$ .

#### E. Sensitivities to efficacy ratios and impulse

Local variations around  $(r_a, r_{\gamma}, J)$  yield

$$\frac{\partial X_{\min}}{\partial r_{\gamma}} = \frac{\delta}{1 - r_a} \gamma_0 \tau, \quad (58)$$

$$\frac{\partial X_{\min}}{\partial r_a} = -\frac{1 - r_{\gamma}}{(1 - r_a)^2} \delta \gamma_0 \tau, \quad (59)$$

$$\frac{\partial X_{\min}}{\partial J} = \kappa \frac{\gamma_0}{a_0} = -\lambda. \quad (60)$$

Equation (60) is the dual interpretation: the (negative) dual slope equals the marginal reduction in  $X$  per additional impulse.

#### F. Optimality gap bounds for mistimed and multi-switch programs

Let  $t$  denote the unique CP  $\rightarrow$  LP switching time and write the switching function (52) near  $t$  as  $S_{\Pi}(t + \Delta t) = \dot{S}_{\Pi}(t) \Delta t + O(\Delta t^2)$ , with  $\dot{S}_{\Pi}(t) > 0$  by Theorem 13. Define

$$m_S := \inf_{|t-t| \leq \Delta} \dot{S}_{\Pi}(t) > 0$$

for some small  $\Delta > 0$ .

**Proposition 15** (Quadratic mistiming penalty). *If the actual switch occurs at  $t + \delta t$  with  $|\delta t| \leq \Delta$  and  $S_{\Pi} \in C^1$  in a neighborhood of  $t$ , then the excess cost satisfies*

$$X - X_{\min} \geq \frac{m_S}{2} (\delta t)^2. \quad (61)$$

**Remark 16** (Regularity requirement). The bound (61) uses a local quadratic expansion of the switching loss; it requires  $S_{\Pi} \in C^1$  near  $t$  (which holds under the smooth closures of Sec. II). This is the condition alluded to as “ $S_{\Pi} \in C^1$  near  $t$ ”.

*Latency budget.* Given an allowable excess  $\Delta X$ , any switch timing error  $|\delta t| \leq \sqrt{2\Delta X/m_S}$  is admissible. Using the bound (53) for  $\dot{S}'_{\Pi}(t)$  we can lower-bound  $m_S$  by  $m_S \geq \alpha C_B - (C_{\Pi B} \|B_x\|/\tau_B + |\lambda^*|(C_a \|\dot{B}_x\| + C_B) + \alpha \|\lambda_B\|/\tau_B)$  along the extremal.

**Proposition 17** (Multi-switch suboptimality). *Let a program perform  $N \geq 2$  switches among  $\Pi \in \{0, 1\}$  while meeting the impulse budget. Then*

$$\begin{aligned} X - X_{\min} &\geq \sum_{j=1}^{N-1} \frac{m_S^{(j)}}{2} (\delta t_j)^2 \\ &\geq \frac{m_S}{2} \sum_{j=1}^{N-1} (\delta t_j)^2, \end{aligned} \quad (62)$$

where  $\delta t_j$  are the deviations of each effective switch from  $t$  when phases are coalesced,  $m_S^{(j)}$  are the local slopes around each surrogate zero, and  $m_S = \min_j m_S^{(j)} > 0$ . In particular, any extra switch strictly increases the cost unless it coincides with  $t$ .

**Remark 18** (Envelope case without memory). If  $B_x$  is absent but the growth has a decreasing envelope  $w(t)$  (e.g., laser envelope), then Hardy–Littlewood rearrangement yields a linear-in-delay penalty

$$\Delta X \geq (\Gamma_{\text{LP}} - \Gamma_{\text{CP}}) \int_0^{\Delta t} [w(t) - w(\tau - t)] dt,$$

with  $\Gamma_{\text{LP}} > \Gamma_{\text{CP}}$  the constant levels in each phase. With memory, the quadratic bound (61) dominates near  $t$ .

**Remark 19** (Monotonicity caveat and fallback). If (26)–(27) fail on a measurable set  $T \subset [0, \tau]$  (e.g., near transparency/ablation), the PMP selector reduces to LP on  $T$  and a single CP→LP switch on  $[0, \tau] \setminus T$ ; feasibility and the dual slope bounds (50) are preserved.

### G. Discussion and integration with Sections II–V

The measure-LP extremality (Theorem 6) and geometric uniqueness (Theorem 10) justify support  $\leq 2$  and identify the two intensity corners as exposed points under Assumption 8. The Pontryagin memory analysis (Theorem 13) then fixes the *order* (CP first), using the inverse-Faraday dynamics (48) and the explicit dominance of  $-\alpha \partial_{B_x} \gamma_{\max}$  over bounded mixed terms (made precise with the dual bound (50)). The switching geometry (55)–(57) connects directly to the Pareto frontier of Sec. V; the sensitivity identity (60) is the basis of the information-price relation (Sec. V). Finally, the gap bounds (61)–(62) quantify the superiority of the single-switch schedule and provide engineering tolerances on timing errors.

## V. PARETO FRONTIERS: MULTI-OBJECTIVE TRADE-OFFS, CONVEXITY, $\varepsilon$ -OPTIMALITY, AND TIME-VARYING EFFICIENCY

We develop the Pareto theory for minimizing integrated instability subject to linear budgets, prove support bounds and convexity, and derive closed-form selection rules when the CP/LP efficacy varies in time. Throughout,  $u(t) = (\Pi(t), I(t))$  takes values in  $U = [0, 1] \times [0, I_{\max}]$ , with the two intensity corners  $u_0 = (0, I_{\max})$  (LP) and  $u_1 = (1, I_{\max})$  (CP) singled out by Lemma 9.

### A. Feasible set, value function, and convexity

Let  $\mathcal{A}$  be the set of occupation measures  $\mu \in \mathcal{P}(U)$  realizable by measurable controls on  $[0, \tau]$ . For  $r \geq 1$  linear budgets, define linear functionals

$$B_j(\mu) = \int_U b_j(u) d\mu(u), \quad j = 1, \dots, r,$$

and the *value function* for the minimization of the integrated growth

$$V(\beta) = \inf \left\{ \int_U \gamma_{\max}(u) d\mu(u) : \mu \in \mathcal{A}, B_j(\mu) = \beta_j, j = 1, \dots, r \right\}. \quad (63)$$

For the basic two-criterion trade-off we take  $r = 1$  with  $b_1 = a$  and  $\beta_1 = \bar{a} = J_0/\tau$ . For multi-objective frontiers we add more linear budgets (e.g., bounds on  $\int \nu_{\text{eff}}(u) d\mu$  or on a surrogate risk).

**Theorem 20** (Convexity, monotonicity, Lipschitzness). *Assume  $\gamma_{\max}, b_j$  are bounded and Borel-measurable on  $U$ . Then:*

1.  $V(\beta)$  is convex on its effective domain and finite on the interior of the budget polytope.
2. For  $r = 1$  with  $b_1 = a$ , the map  $J \mapsto X_{\min}(J) = \tau V(J/\tau)$  is nonincreasing, convex, and  $L$ -Lipschitz with  $L = \tau(\gamma_U - \gamma_L)/(a_U - a_L)$ .
3. The subgradient set  $\partial X_{\min}(J)$  is the (nonempty) interval of optimal dual slopes  $\{-\lambda\}$ ; when exposed faces are unique (Theorem 10),  $X_{\min}$  is differentiable with  $X'_{\min}(J) = -\lambda(J)$ .

*Proof sketch.* (i) and (ii) follow from LP duality and the convexity of the feasible set  $\{\mu : B_j(\mu) = \beta_j\}$ ; the Lipschitz constant comes from the dual bound (50). (iii) is standard sensitivity for parametric LPs; uniqueness of the exposed face gives single-valued subgradient.  $\square$

### B. Support size under multiple budgets

**Theorem 21** (Support bound under  $r$  budgets). *Under the hypotheses of Theorem 20, there exists an optimal measure  $\mu$  with  $\text{supp}(\mu) \leq r + 1$ .*

*Proof.* This is Carathéodory's theorem for moment problems on compact sets: the optimal extreme point of the feasible moment polytope has support size at most  $r + 1$ .  $\square$

**Corollary 22** (Geometry for  $r = 2$ ). *With two budgets, optimal solutions lie on triangles of  $\text{co}(S)$  where  $S = \{(b_1(u), b_2(u), \gamma_{\max}(u)) : u \in U\}$ ; the Pareto surface is piecewise planar.*

### C. Two-corner frontier and affine segments

Specializing to the intensity corners  $u_0, u_1$  as in Sec. IV D, define

$$\begin{aligned} r_a &= \frac{a_1}{a_0} \in (0, 1], \\ r_\gamma &= \frac{\gamma_1}{\gamma_0} \in (0, 1), \\ \delta &= 1 - \frac{J}{a_0 \tau} \in [0, 1 - r_a]. \end{aligned} \quad (64)$$

Then the frontier is the affine segment

$$\frac{X_{\min}(J)}{\gamma_0 \tau} = 1 - \kappa \delta, \quad \kappa = \frac{1 - r_\gamma}{1 - r_a}, \quad (65)$$

with dual slope

$$\lambda(J) = -\frac{dX_{\min}}{dJ} = -\frac{\gamma_0}{a_0} \kappa. \quad (66)$$

When additional corners are available (e.g., intermediate ellipticities or intensity shaping), the global frontier is the lower convex envelope of the corresponding affine pieces and is *piecewise linear* and convex in  $J$ .

#### D. Time-varying efficacy: continuous knapsack and threshold rule

Suppose the relative CP/LP differences vary in time through *known* functions

$$\Delta a(t) = a_1(t) - a_0(t) < 0, \quad \Delta \gamma(t) = \gamma_1(t) - \gamma_0(t) < 0, \quad (67)$$

with  $a_i, \gamma_i$  measurable and bounded. We seek a measurable selector  $p(t) \in \{0, 1\}$  indicating CP use to satisfy

$$\int_0^\tau (a_0(t) + p(t)\Delta a(t)) dt = J,$$

and to minimize

$$X = \int_0^\tau (\gamma_0(t) + p(t)\Delta \gamma(t)) dt.$$

Define the *efficiency score*

$$e(t) := \frac{-\Delta \gamma(t)}{-\Delta a(t)} \in [0, \infty), \quad (68)$$

interpreted as stability gain per unit impulse penalty.

**Theorem 23** (Threshold rule and uniqueness). *There exists a unique  $\lambda < 0$  such that the selector*

$$p(t) = \mathbf{1}\{e(t) > -\lambda\}, \quad (69)$$

*achieves the impulse budget and minimizes  $X$ . Moreover, the mapping*

$$\lambda \mapsto \int_0^\tau (a_0(t) + \mathbf{1}\{e(t) > -\lambda\}\Delta a(t)) dt$$

*is strictly increasing and continuous, ensuring existence and uniqueness of  $\lambda$ .*

**Monotonicity fallback.** *If the monotonicity inequalities (26) fail on a measurable set  $\mathcal{T} \subset [0, \tau]$  (e.g. near transparency or ablation), the pointwise selector reduces to  $p^*(t) = 0$  on  $\mathcal{T}$  and applies the threshold rule on  $[0, \tau] \setminus \mathcal{T}$ ; feasibility and optimality of  $X$  are preserved for the modified budget.*

*Proof sketch.* Lagrangian relaxation gives the pointwise minimization of  $\Delta \gamma + \lambda \Delta a$ , selecting CP where  $\Delta \gamma + \lambda \Delta a < 0$ , i.e., where  $e(t) > -\lambda$ . Monotonicity in  $\lambda$  follows since  $\Delta a < 0$  and the superlevel sets  $\{e > -\lambda\}$  expand with  $\lambda$ .  $\square$

**Remark 24** (Order and realizability). In the envelope-only case (no magnetization memory), rearrangement implies any measurable  $p$  can be realized as a *single* contiguous CP block (or a finite union) without changing  $(J, X)$ . With memory (Sec. IV C), Pontryagin enforces a *single* CP $\rightarrow$ LP switch and modifies the effective score via  $B_x$ -dependence; the same threshold principle applies to the augmented Hamiltonian.

*Fallback outside monotonicity.* If the inequalities (26)–(27) fail on a measurable set  $\mathcal{T} \subset [0, \tau]$  (e.g. near transparency or ablation), set  $p(t) = 0$  on  $\mathcal{T}$  and apply the threshold rule on  $[0, \tau] \setminus \mathcal{T}$ ; feasibility and optimality for the modified budget follow from the pointwise Lagrangian argument. (See Sec. II.E for formal monotonicity conditions.)

#### E. $\epsilon$ -optimal solutions: discretization and quantization bounds

Let  $\mathcal{T}_N = \{t_j = j\tau/N\}_{j=0}^N$  and form the Riemann approximation choosing  $p_N$  constant on each bin, with the sorted-by-score selection until the discrete impulse meets  $J$  within tolerance  $\Delta J_N$ .

**Proposition 25** (Discretization gap). *Assume  $a_i, \gamma_i \in L^\infty(0, \tau)$  and  $\Delta a \leq -a_{\min} < 0$ . Then the discretized threshold schedule satisfies*

$$0 \leq X[p_N] - X[p] \leq |\lambda| \Delta J_N \leq \frac{|\lambda| \tau \|\Delta a\|_\infty}{N}. \quad (70)$$

*Proof.* Value function convexity implies  $X(J + \Delta J) \leq X(J) + |\lambda| \Delta J$ . The Riemann error for the impulse integral is  $O(\|\Delta a\|_\infty \tau/N)$ .  $\square$

**Corollary 26** (CP fraction quantization). *If only a single switch is allowed (Sec. IV C), quantizing the CP fraction to  $\tilde{p}$  with  $|p - \tilde{p}| \leq 1/N$  yields*

$$0 \leq X(\tilde{p}) - X(p) \leq |\lambda| a_0 \tau |p - \tilde{p}| \leq \frac{|\lambda| a_0 \tau}{N}. \quad (71)$$

#### F. Multi-objective frontiers and curvature

Add linear budgets  $B_2(\mu) = \int \nu_{\text{eff}}(u) d\mu(u)$  (viscous budget) and  $B_3(\mu) = \int \zeta(u) d\mu(u)$  (EoT proximity). The  $(J, \mathcal{V}, X)$  frontier is the lower boundary of the convex hull of

$$\{(a(u), \nu_{\text{eff}}(u), \gamma_{\max}(u)) : u \in U\}.$$

By Theorem 21, optimal measures have  $\text{supp} \leq 3$ ; the frontier is a piecewise ruled surface whose curvature changes only at transitions between triangle faces. If the budget normals are in general position, exposed faces are unique and the frontier is  $C^1$  except at finitely many budget values (kinks).

#### G. Information price of impulse (link to Sec. VI)

Let  $X_{\text{th}}$  be a failure threshold on the log-amplitude and suppose the jump-diffusion of Sec. VI yields the Cher-

noff-Gaussian tail bound

$$\mathbb{P}\left[\sup_{t \leq \tau} X_k(t) \geq X_{\text{th}}\right] \lesssim \exp\left(-\frac{(X_{\text{th}} - X_0 - X_{\min}(J))^2}{2 \Sigma_k}\right), \quad (72)$$

with  $\Sigma_k = \int_0^\tau \sigma_k^2 dt$  (mode-dependent) and  $X_0 = \ln|\eta_k(0)|$ . Differentiating (72) along the Pareto frontier gives the *information price* identity

$$\frac{d}{dJ} \log \mathbb{P}[\text{breakup at } k] = -\lambda(J) \times \frac{X_{\text{th}} - X_0 - X_{\min}(J)}{\Sigma_k}, \quad (73)$$

where  $-\lambda(J) = dX_{\min}/dJ$  by Theorem 20. Thus each unit of impulse budget buys an exponential factor governed by the dual slope and the remaining “distance to threshold.” (For the jump-diffusion full Chernoff bound and  $\Sigma_k$  construction, see Sec. VI.)

## H. Practical extraction and algorithms

These algorithms are relevant for practical pulse-shaping and programmability [18, 19], and can be implemented in closed-loop optimization systems [20].

*A. Two-corner (CP/LP) planner.* Estimate  $(a_0, a_1, \gamma_0, \gamma_1)$  at  $I_{\max}$  (with the C-factors of Sec. II D), compute  $\kappa = (1 - r_\gamma)/(1 - r_a)$ ; if  $J \leq a_1 \tau$  choose all-CP; else set  $p = \delta/(1 - r_a)$  with  $\delta = 1 - J/(a_0 \tau)$  and schedule a single CP→LP switch at  $t = p\tau$  (Sec. IV C).

*B. Time-varying (continuous knapsack).* Compute  $e(t)$  by (68), sort bins by  $e$ , and fill until the impulse matches  $J$ . The dual  $\lambda$  is the threshold  $-\lambda$  separating selected bins.

*C.  $\varepsilon$ -optimality via coarse bins.* Pick  $N$  such that the desired gap  $\varepsilon$  satisfies  $\varepsilon \geq |\lambda| \tau \|\Delta a\|_\infty / N$  (Prop. 25); use a single CP block (or one switch with memory) of length  $\tilde{p}\tau$ , quantized to within  $1/N$  (Cor. 71).

*D. Multi-objective (three budgets).* Enumerate triangle faces from a finite library of candidate controls (e.g., CP, LP, and one elliptic state), evaluate face normals against  $(J, \mathcal{V})$ , and pick the exposed face containing the target budget point.

*Computational cost.* The time-varying selector (Sec. V.D) sorts  $N$  time bins by score  $e(t)$  and is  $O(N \log N)$ ; with a single Pontryagin switch, we need only one threshold and one cut (linear time).

The results of this section provide the global trade-space and its computationally light selectors, and they connect directly to robustness (Sec. VII) and stochastic risk (Sec. VI) through the dual slope  $-\lambda(J)$ .

TABLE II. Calibration constants extracted from LP/CP pair measurements. Values are least-squares fits to LP/CP pairs using the Sec. III.F extractor; uncertainties are 95% CIs from the Jacobian propagation (Prop. 5').

Parameter	Symbol	Prior Range	Fitted Value
QM viscosity	$C_{\text{QM}}$	[0.3, 3]	$1.2 \pm 0.4$
IF viscosity	$C_{\text{IF}}$	[0.3, 3]	$0.8 \pm 0.3$
SAM fraction	$\alpha$	$[10^{-4}, 10^{-3}]$ T·s/W	$(2.1 \pm 0.7) \times 10^{-4}$ T·s/W
B-field time	$\tau_B$	[20, 100] fs	$50 \pm 20$ fs

## VI. STOCHASTIC ANALYSIS FROM QED PHOTON STATISTICS

We derive the stochastic evolution of each unstable mode from QED photon emission (shot noise), radiation-reaction (RR) recoil, and pair bursts. The observable is the *log-amplitude*

$$X_k(t) := \ln|\eta_k(t)|, \quad X_k(0) = X_{k,0}. \quad (74)$$

In the linear window  $dX_k/dt = \gamma_k + \text{stochastic terms}$ . We quantify diffusion and jumps from microphysics, formulate the Fokker-Planck equation, give first-passage distributions, and derive Chernoff/large-deviation bounds that connect to the Pareto “information price” in Sec. V.

### A. Sensitivities and validity band

For the thin-foil dispersion

$$\gamma^2 + 2\nu k^2 \gamma = a k - T k^3, \quad T = \sigma_s / \rho,$$

the partial derivatives along the growing branch are

$$\frac{\partial \gamma}{\partial a} = \frac{k}{2(\gamma + \nu k^2)}, \quad (75)$$

$$\frac{\partial \gamma}{\partial T} = -\frac{k^3}{2(\gamma + \nu k^2)}, \quad (76)$$

$$\frac{\partial \gamma}{\partial \nu} = \frac{\nu k^4}{\gamma + \nu k^2} - k^2. \quad (77)$$

**Validity.** These require  $\gamma + \nu k^2 \neq 0$ , i.e.,  $k \in (0, k_T)$  where  $\gamma > 0$  (cf. Sec. III); at neutral stability ( $k = 0$  or  $k = k_T$ ), the sensitivity form is singular and a separate boundary analysis is needed.

**Sign.** In the growing band,  $\partial \gamma / \partial \nu = \nu k^4 / (\gamma + \nu k^2) - k^2 = -(\gamma k^2) / (\gamma + \nu k^2) < 0$ .

### B. Photon shot noise and diffusion intensity

Photon arrival is Poisson with rate

$$\Lambda_\gamma = \frac{\mathcal{R} I A}{\hbar \omega_0},$$

and each reflected photon transfers  $2\hbar k_0$  momentum, producing pressure fluctuations. The resulting *acceleration* noise (per unit time) on an areal mass  $\sigma$  over area  $A$  has variance rate

$$D_a = \text{Var} \left[ \frac{\Delta p}{\sigma \Delta t} \right] = \frac{(2\hbar k_0)^2 \Lambda_\gamma}{\sigma^2 A^2} = \frac{4\hbar\omega_0}{c^2} \frac{\mathcal{R} I}{\sigma^2 A}. \quad (78)$$

Similarly, fluctuations in  $T$  and  $\nu$  can be included (typically subleading in the opaque, near-normal regime). Propagating through the sensitivities (75) yields the diffusion coefficient of  $X_k$ :

$$\sigma_k^2(t) = S_a^2 D_a + S_T^2 D_T + S_\nu^2 D_\nu + 2S_a S_T D_{aT} + \dots, \quad (79)$$

where  $S_a = \partial\gamma/\partial a$ ,  $S_T = \partial\gamma/\partial T$ ,  $S_\nu = \partial\gamma/\partial\nu$  from (75),  $D_T, D_\nu$  are variance rates of  $T, \nu$  (including RR and microturbulence), and cross-covariances like  $D_{aT}$  are often negligible. Equation (78) implies a favorable SNR scaling for larger  $A$  and  $\sigma$ .

### C. RR emission and pair bursts: jump contributions

RR emission modulates  $a$  (via momentum recoil) and effective transport coefficients; pair bursts (when  $\chi_e$  is large) inject discontinuous changes in  $\rho$  and thus  $T = \sigma_s/\rho$ , and can transiently alter  $\nu$ . These jump-diffusion tails become important near cascade limits [21], as reviewed in [16, 17]. Let  $N_\pm$  be compound Poisson processes with intensities  $\Lambda_\pm$  for pair creation/annihilation channels. To leading order, a single event produces a jump in  $\gamma_k$  of size

$$\Delta\gamma_k \approx S_a \Delta a + S_T \Delta T + S_\nu \Delta\nu,$$

where  $\Delta a, \Delta T, \Delta\nu$  are the parameter changes caused by the event (sign and magnitude determined by the channel). The *Lévy measure* of  $X_k$  therefore is

$$\nu_k(dz) = \Lambda_+ \mathbb{P}[\Delta\gamma_k \in dz \mid \text{pair event } +] + \Lambda_- \mathbb{P}[\Delta\gamma_k \in dz \mid \text{pair event } -]. \quad (80)$$

*Parametrization and variance inflation.* We adopt a two-point mixture for pair events with  $z_\pm = S_T \Delta T_\pm + S_\nu \Delta\nu_\pm + S_a \Delta a_\pm$  and rates  $\Lambda_\pm(\chi_e, I)$ :

$$\nu_k(dz) = \Lambda_+ \delta_{z_+}(dz) + \Lambda_- \delta_{z_-}(dz), \quad (81)$$

$$\int z^2 \nu_k(dz) = \Lambda_+ z_+^2 + \Lambda_- z_-^2.$$

The bound (89) holds with variance inflation  $\Sigma_k \mapsto \Sigma_k + \int z^2 \nu_k(dz)$ . For  $\chi_e \ll 1$  we set  $\Lambda_\pm \rightarrow 0$ .

**Bound-level identity.** The “information-price” derivative follows from a tail bound (Doob/Chernoff), not from the exact hitting probability; it is therefore conservative, especially in the presence of jumps.

*Jump parametrization and timescale separation.* We parameterize pair/recoil bursts via a two-point Lévy measure  $\nu_k(dz) = \Lambda_+(\chi_e, I) \delta_{z_+}(dz) + \Lambda_-(\chi_e, I) \delta_{z_-}(dz)$  with  $z_\pm = S_T \Delta T_\pm + S_\nu \Delta\nu_\pm + S_a \Delta a_\pm$ . For  $\chi_e \ll 1$  we set  $\Lambda_\pm \rightarrow 0$  (diffusive limit). The sensitivity propagation assumes  $\tau_{\text{noise}} \ll \gamma^{-1}$  (linear RTI window), valid for photon shot noise and rare compound-Poisson pair bursts. The “information-price” identity is derived from a Chernoff/Doob tail bound and is therefore conservative in the presence of strong mode coupling.

For bookkeeping in the diffusion matrix, we also define the RR-induced diffusion in  $a$  from discrete photon emission (beyond shot noise treated in (78)) by

$$D_a^{\text{RR}} = (n_e d) \frac{1}{(\sigma A)^2} \int m_2^{\parallel}(\chi_e) W_\gamma(\varepsilon; \chi_e) d\varepsilon,$$

with  $W_\gamma$  the photon emission rate density and  $m_2^{\parallel}$  the *longitudinal second moment per event* (denoted  $m_2$  in earlier shorthand).

### D. Jump–diffusion SDE for the log-amplitude

Collecting the continuous (diffusion) and discontinuous (jump) components, we write the *jump–diffusion* SDE

$$dX_k(t) = \gamma_k(t) dt + \sigma_k(t) dW_t + \int_{\mathbb{R}} z \tilde{N}_k(dt, dz), \quad (82)$$

where  $\sigma_k^2$  is given by (79),  $W_t$  is standard Brownian motion, and  $\tilde{N}_k$  is the compensated Poisson random measure with Lévy measure  $\nu_k(dz)$  from (80). The integrated drift and diffusion are

$$\Gamma_k(t) := \int_0^t \gamma_k(s) ds, \quad \Sigma_k(t) := \int_0^t \sigma_k^2(s) ds. \quad (83)$$

*Decoherence correction (phase noise).* If the drive carries a fast phase  $\phi$  with  $\langle\phi\rangle = 0$ ,  $\langle\phi^2\rangle = \sigma_\phi^2 t$  and multiplicatively modulates the gain, the Wong–Zakai/Stratonovich-to-Itô correction yields an effective *drift reduction*

$$\gamma_k \mapsto \gamma_k - \frac{1}{2} \sigma_\phi^2(t), \quad (84)$$

i.e., a decoherence penalty of  $\sigma_\phi^2/2$  in the log-amplitude drift.

### E. Fokker–Planck equation and diffusion limit

Neglecting jumps, the PDF  $p(x, t)$  of  $X_k$  solves

$$\partial_t p(x, t) = -\partial_x (\gamma_k(t) p) + \frac{1}{2} \partial_{xx} (\sigma_k^2(t) p). \quad (85)$$

For constant coefficients ( $\gamma_k \equiv \bar{\gamma}$ ,  $\sigma_k \equiv \bar{\sigma}$ ),  $X_k$  is Gaussian with mean  $X_{k,0} + \bar{\gamma}t$  and variance  $\bar{\sigma}^2 t$ . Let



$x_{\text{th}} > X_{k,0}$  be a failure threshold. The *first-passage time*  $T$  to  $x_{\text{th}}$  is inverse-Gaussian,

$$T \sim \text{IG}(\mu, \lambda), \quad (86)$$

$$\mu = \frac{x_{\text{th}} - X_{k,0}}{\bar{\gamma}}, \quad \lambda = \frac{(x_{\text{th}} - X_{k,0})^2}{\bar{\sigma}^2}.$$

with mean  $\mathbb{E}[T] = \mu$  and variance  $\text{Var}[T] = \mu^3/\lambda$ . If  $\bar{\gamma} \leq 0$  the mean FPT diverges, consistent with stability.

### F. Large deviations and Chernoff bounds

For the diffusion model, the reflection principle implies

$$\begin{aligned} \mathbb{P}\left[\sup_{s \leq t} X_k(s) \geq x\right] &= \mathbb{P}[X_k(t) \geq x] \exp\left(\frac{2\bar{\gamma}}{\bar{\sigma}^2}(x - X_{k,0})\right) \\ &\leq \exp\left(-\frac{(x - X_{k,0} - \bar{\gamma}t)^2}{2\bar{\sigma}^2 t}\right). \end{aligned} \quad (87)$$

More generally, for the jump–diffusion (82), define the c.g.f. per unit time via the Lévy–Khintchine exponent

$$\begin{aligned} \psi(\theta; t) &= \theta \gamma_k(t) + \frac{1}{2} \theta^2 \sigma_k^2(t) \\ &\quad + \int_{\mathbb{R}} (e^{\theta z} - 1 - \theta z \mathbf{1}_{\{|z| < 1\}}) \nu_k(dz, t). \end{aligned} \quad (88)$$

Then the exponential supermartingale  $M_t = \exp\{\theta X_k(t) - \int_0^t \psi(\theta; s) ds\}$  yields, by Doob’s inequality, for any  $\theta \geq 0$ ,

$$\mathbb{P}\left[\sup_{s \leq t} X_k(s) \geq x\right] \leq \exp\left(-\theta x + \int_0^t \psi(\theta; s) ds\right). \quad (89)$$

Optimizing over  $\theta$  gives the large-deviation rate function  $I(y) = \sup_{\theta \geq 0} \{\theta y - \bar{\psi}(\theta)\}$  with  $\bar{\psi}(\theta) = t^{-1} \int_0^t \psi(\theta; s) ds$ . In the diffusion-only case ( $\nu_k \equiv 0$ ) (89) reduces to the Gaussian bound

$$\mathbb{P}\left[\sup_{s \leq t} X_k(s) \geq x\right] \leq \exp\left(-\frac{(x - X_{k,0} - \Gamma_k(t))^2}{2 \Sigma_k(t)}\right), \quad (90)$$

with  $\Gamma_k, \Sigma_k$  from (83). We record this as:

**Theorem 27** (Chernoff–Gaussian tail bound). *For any  $t \leq \tau$  and mode  $k$  in the growing band,*

$$\mathbb{P}\left[\sup_{s \leq t} X_k(s) \geq x_{\text{th}}\right] \leq \exp\left(-\frac{(x_{\text{th}} - X_{k,0} - \Gamma_k(t))^2}{2 \Sigma_k(t)}\right).$$

The bound is conservative in the presence of upward jumps (pairs); the general bound (89) should be used when  $\nu_k \neq 0$ .

### G. Crossing-time distributions beyond diffusion

With jumps, explicit FPT laws are rarely closed-form. Two practical approaches are: (i) *exponential tilting* via (89) to bound the survival function  $\mathbb{P}[T > t]$ ; (ii) *diffusion approximation* for small jumps ( $\int z^2 \nu_k(dz) \ll \bar{\sigma}^2$ ), which corrects  $\bar{\sigma}^2 \mapsto \bar{\sigma}^2 + \int z^2 \nu_k(dz)$  and uses (86). In both cases, the design-relevant statistic is the *exponential tail* controlled by the rate function  $I(\cdot)$ .

### H. Design-level aggregation and link to Pareto information price

For a failure threshold  $x_{\text{th}}$ , the diffusion bound (90) implies

$$\log \mathbb{P}[\text{breakup at } k] \lesssim -\frac{(x_{\text{th}} - X_{k,0} - X_{\min}(J))^2}{2 \Sigma_k}, \quad (91)$$

assuming the controller realizes  $X_{\min}(J) = \Gamma_k(\tau)$  (Pareto-optimal schedule). Differentiating in  $J$  along the frontier gives the identity

$$\frac{d}{dJ} \log \mathbb{P}[\text{breakup at } k] = -\lambda(J) \times \frac{x_{\text{th}} - X_{k,0} - X_{\min}(J)}{\Sigma_k}, \quad (92)$$

with  $-\lambda(J) = dX_{\min}/dJ$  (Sec. V). Equation (92) is the *information-theoretic price of impulse* advertised in Sec. V G.

### I. Summary for implementation

- **Compute**  $S_a, S_T, S_\nu$  from (75) at each  $(k, t)$  under the chosen control; restrict to  $k \in (0, k_T)$ .
- **Assemble**  $\sigma_k^2 = S_a^2 D_a + \dots$  via (78)–(79), add RR diffusion  $D_a^{\text{RR}}$  and, if needed, small-jump variance  $\int z^2 \nu_k(dz)$ .
- **Evaluate**  $\Gamma_k, \Sigma_k$  from (83); use Theorem 27 for a conservative failure bound (or (89) if jumps are non-negligible).
- **Propagate** the bound through the Pareto frontier using (92) to quantify how added impulse budget reduces risk exponentially.
- **Account** for decoherence via (84) (phase noise penalty).

*Mode coupling.* Inter-mode coupling increases the effective variance; our tail bounds remain conservative by coarse-graining to blocks and replacing  $\Sigma_k$  with  $\text{tr } \Sigma_{\text{block}}$  in (90).

## VII. MINIMAX ROBUSTNESS: ENDPOINT ADVERSARIES, WORST-CASE SLOPES, AND NORM BOUNDS

We study robustness to bounded modeling error and parametric uncertainty in the static maps  $a(u)$  and  $\gamma_{\max}(u)$  used by the controller. The decision variable is an occupation measure  $\mu \in \mathcal{P}(U)$  (Sec. IV). The adversary picks  $a, \gamma$  from a convex compact uncertainty set  $\mathcal{U}$ ; for concreteness, we use hyperrectangles preserving monotonicity:

$$a(u) \in [a_L(u), a_U(u)], \quad \gamma_{\max}(u) \in [\gamma_L(u), \gamma_U(u)]. \quad (93)$$

The saddle-point problem is

$$\inf_{\mu \in \mathcal{P}(U)} \sup_{(a, \gamma) \in \mathcal{U}} \int_U \gamma(u) d\mu(u) \quad \text{s.t.} \quad \int_U a(u) d\mu(u) = \bar{a}. \quad (94)$$

### A. Sion's theorem and endpoint structure

**Theorem 28** (Minimax and endpoint adversaries). *Under the uncertainty set defined in (93), the minimax game (94) admits a value and a saddle point. Moreover, an optimal adversary selects endpoint functions  $(a^\#, \gamma^\#)$  a.e. on  $U$ , i.e.  $a^\#(u) \in \{a_L(u), a_U(u)\}$  and  $\gamma^\#(u) \in \{\gamma_L(u), \gamma_U(u)\}$ . Under Assumption 8, the controller's optimal  $\mu$  has support  $\leq 2$  on the intensity corners.*

*Proof sketch.* Bilinearity in  $(\mu, (a, \gamma))$ , convex compact feasible sets, and continuity imply Sion's minimax theorem applies. Extreme points of  $\mathcal{U}$  are the endpoints; extreme points of the controller's feasible moment set have support size  $\leq 2$  (Carathéodory).  $\square$

### B. Worst-case slope and feasibility checks

Let the relevant exposed points be  $u_0 = (0, I_{\max})$  and  $u_1 = (1, I_{\max})$  with intervals

$$a_i \in [a_{i,L}, a_{i,U}], \quad \gamma_i \in [\gamma_{i,L}, \gamma_{i,U}], \quad i \in \{0, 1\},$$

and  $a_1 < a_0$  (CP has no larger impulse than LP at  $I_{\max}$ ). The adversary maximizes the slope of the supporting line.

$$\lambda_{\text{wc}} = \sup \left\{ -\frac{\gamma_1 - \gamma_0}{a_1 - a_0} : a_i \in [a_{i,L}, a_{i,U}], \gamma_i \in [\gamma_{i,L}, \gamma_{i,U}], a_1 < a_0 \right\}. \quad (95)$$

**Feasibility.** If the intervals overlap so that  $a_{1,U} \geq a_{0,L}$ , then the two-corner construction may violate  $a_1 < a_0$ ; either (i) switch to an alternative exposed pair with  $a_1 < a_0$ , or (ii) conclude that the impulse budget  $J$  near  $a_1\tau$  is infeasible (requires an intersection test on  $\text{co}(S)$ ).

### C. Robust frontier and support

Let  $X_{\min}^{\text{rob}}(J)$  be the value of (94). Then on any exposed segment,

$$\frac{d}{dJ} X_{\min}^{\text{rob}}(J) = -\lambda_{\text{wc}}. \quad (96)$$

The robust optimal control remains two-point and (with magnetization memory) single-switch CP $\rightarrow$ LP (Theorem 13), now sized by the worst-case ratios  $(r_a, r_\gamma)$  consistent with (93).

### D. Norm bounds and $H_\infty$ view

Aggregate parametric disturbances as  $d_\gamma(t)$  and  $d_a(t)$ :

$$\gamma(t) = \gamma_{\text{nom}}(t) + d_\gamma(t), \quad a(t) = a_{\text{nom}}(t) + d_a(t).$$

The cost perturbation obeys

$$\Delta X = \int_0^\tau d_\gamma(t) dt + \lambda(J) \int_0^\tau d_a(t) dt, \quad (97)$$

giving the  $L_1$  bound  $|\Delta X| \leq \|d_\gamma\|_{L_1} + |\lambda| \|d_a\|_{L_1}$ . For  $L_2$  disturbances,

$$|\Delta X| \leq \sqrt{\tau} \|d_\gamma\|_{L_2} + |\lambda| \sqrt{\tau} \|d_a\|_{L_2}. \quad (98)$$

These are static  $H_\infty$  gains from  $(d_\gamma, d_a)$  to  $\Delta X$  with diagonal gain vector  $(\sqrt{\tau}, |\lambda|\sqrt{\tau})$ .

### E. Static $\mu$ -analysis

For structured, independent interval uncertainties  $\Delta = \text{diag}(\Delta_\gamma, \Delta_a)$  with  $|\Delta_\gamma| \leq 1$ ,  $|\Delta_a| \leq 1$ , the robust margin is captured by the static structured singular value

$$\mu_{\text{static}}(G) = \left( \min\{\|\Delta\| : \det(I - G\Delta) = 0\} \right)^{-1}, \quad (99)$$

$$\text{where } G = \begin{bmatrix} \sqrt{\tau} & 0 \\ 0 & |\lambda|\sqrt{\tau} \end{bmatrix}.$$

Since there is no frequency dependence,  $\mu_{\text{static}}$  reduces to the  $L_2$  bound (98); dynamic weighting would require full  $\mu$ -analysis, which we do not need here.

Equations (95)–(98) close the robustness loop: the adversary's endpoint structure mirrors the controller's two-point structure; the robust slope  $-\lambda_{\text{wc}}$  is the worst-case “information price” used in Sec. V.

## VIII. EDGE-OF-TRANSPARENCY TRACKING: DELAY-ROBUST ISS AND DEADBAND

We design a feedback law that tracks the edge of relativistic transparency [5] with a guardband, despite actuation and measurement delays.

### A. Plant, measurement, and controller

Let  $\zeta$  be the transparency surrogate (e.g., areal density or a calibrated proxy) and  $a_0$  the normalized drive amplitude. The plant obeys

$$\dot{\zeta}(t) = -\frac{1}{\tau_\zeta} \zeta(t) + g u(t - \tau_a), \quad y(t) = \frac{\zeta(t - \tau_m)}{a_0(t - \tau_m)} + n(t), \quad (100)$$

with time constant  $\tau_\zeta > 0$ , gain  $g > 0$ , actuation delay  $\tau_a \geq 0$ , measurement delay  $\tau_m \geq 0$ , and additive noise  $n(t)$ . The setpoint is the guardband ratio  $s^* = 1 + \varepsilon > 1$ . Feedforward:

$$u_{\text{ff}}(t) = \frac{1}{g\tau_\zeta} (1 + \varepsilon) a_0(t). \quad (101)$$

Feedback (error on the delayed measurement):

$$\begin{aligned} e(t) &= \frac{\zeta(t - \tau_m)}{a_0(t - \tau_m)} - (1 + \varepsilon), \\ u(t) &= u_{\text{ff}}(t) - K \hat{e}(t), \\ \hat{e}(t) &= \text{sat}_\Delta(e(t)), \end{aligned} \quad (102)$$

where  $\text{sat}_\Delta$  is a symmetric deadband (no action for  $|e| \leq \Delta$ ).

### B. Closed-loop error dynamics and stability

Linearizing the ratio around  $s^*$  and absorbing higher-order terms into a disturbance  $w(t)$  gives

$$\begin{aligned} \dot{e}(t) &= -\alpha e(t) - \beta e(t - \tau_d) + w(t), \\ \text{where } \alpha &= \frac{1}{\tau_\zeta}, \quad \beta = gK, \quad \tau_d = \tau_a. \end{aligned} \quad (103)$$

(Measurement delay enters  $w(t)$  additively via finite-difference approximations of  $a_0$ .) The characteristic equation is  $s + \alpha + \beta e^{-s\tau_d} = 0$ .

**Theorem 29** (Delay-independent exponential ISS). *If  $0 < gK < 1/\tau_\zeta$  (i.e.,  $0 < \beta < \alpha$ ), then for any  $\tau_d \geq 0$  the origin of (103) is exponentially stable, and the input-to-state bound*

$$|e(t)| \leq e^{-ct} \|e_0\|_\infty + \frac{1}{c} \sup_{s \leq t} |w(s)|, \quad (104)$$

$$\text{where } c = \alpha - \beta = \frac{1}{\tau_\zeta} - gK,$$

holds.

*Proof sketch.* This is a Hayes-type delay-independent condition for the scalar DDE  $x' + \alpha x + \beta x(t - \tau) = 0$ : the sector  $0 < \beta < \alpha$  implies uniform exponential stability for all  $\tau \geq 0$ . ISS follows by variation of constants.  $\square$

### C. Disturbance budget and deadband

Let the envelope slew be bounded by  $|\dot{a}_0| \leq L_{a_0}$  and  $a_0(t) \geq a_{0,\min} > 0$ . Then one can bound the effective disturbance as

$$\|w\|_\infty \leq c_w \equiv \left( \frac{\tau_a}{\tau_\zeta} + 1 + \varepsilon \right) \frac{L_{a_0}}{a_{0,\min}} + \|n\|_\infty. \quad (105)$$

With a deadband  $\Delta \geq \|n\|_\infty$ , the ultimate bound becomes

$$\limsup_{t \rightarrow \infty} |e(t)| \leq \frac{c_w}{c} + \Delta, \quad c = \frac{1}{\tau_\zeta} - gK. \quad (106)$$

If saturation  $u \in [u_{\min}, u_{\max}]$  binds, the two-level variant uses  $u \in \{u_{\min}, u_{\max}\}$ ; feasibility is decided by whether  $J$  is achievable at the bound (Sec. V).

Equations (104)–(106) quantify the trade between tracking accuracy (large  $c$ ) and noise rejection (large  $\Delta$ ), and they are delay-robust provided  $0 < gK < 1/\tau_\zeta$ .

**Remark (conservatism).** The delay-independent condition  $0 < gK < 1/\tau_\zeta$  is conservative; less restrictive delay margins can be obtained with Lyapunov–Krasovskii functionals. We keep the Hayes sector for transparency and because it yields closed-form ISS bounds (104)–(106). The sector  $0 < gK < 1/\tau_\zeta$  ensures stability for any actuation delay; tuning  $K$  sets the steady-state error via (106).

*Scaling of  $X$  under edge tracking.* With  $k_T = \sqrt{a/T}$ , the stability cost scales as  $X \sim \int \sqrt{a} k_T dt = \int a^{3/4} T^{-1/4} dt$ . Under active tracking with  $s = \zeta/a_0 = 1 + \varepsilon$  (constant),  $a \propto a_0$  and thus

$$X \propto \int a_0^{3/4} T^{-1/4} dt \quad (\text{if } T \text{ weakly varying}). \quad (107)$$

If  $T(\zeta) \propto \zeta^q$ , then  $X \propto \int a_0^{3/2} \zeta^{-(3+q)/4} dt$ , recovering (107) at  $q = 0$ .

**On  $(g, \tau_\zeta)$ .** The gain  $g$  represents the actuation map from command  $u$  to the  $\zeta$  surrogate (calibrated pre-shot);  $\tau_\zeta$  captures the effective relaxation. The delay-independent sector  $0 < gK < 1/\tau_\zeta$  is conservative; less restrictive margins can be obtained by Lyapunov–Krasovskii functionals (see, e.g., Hale and Verduyn Lunel, *Introduction to Functional Differential Equations*, 1993).

## IX. MODE-KILLER DESIGN: INVERSE SIZING, TOLERANCES, AND MULTI-MODE QP

We recall the inverse sizing from Sec. II for structured targets [6–8]. For a thickness ripple  $d(y) = d_0 + \delta d \cos(ky)$ ,

$$\frac{\partial \sigma_s}{\partial d} \delta d = \frac{\rho a}{(k)^2} \implies \delta d = \frac{\rho a}{(k)^2 (\partial \sigma_s / \partial d)}. \quad (108)$$

A damping margin  $\gamma_m < 0$  at  $k$  gives the tolerance

$$|\Delta(\delta d)| \leq \frac{2\rho\mu|\gamma_m|}{k^3|\partial\sigma_s/\partial d|} \left(1 + \frac{\nu_{\text{eff}} k^2}{|\gamma_m|}\right), \quad (109)$$

where  $\mu \in (0, 1)$  is a design fraction and the viscous factor accounts for  $\partial\gamma/\partial\sigma_s$  through (34).

### A. Multi-mode suppression as a convex QP

Target modes  $\{k_n\}_{n=1}^N$  with desired margins  $\{\gamma_{m,n}\}$ . Linearize

$$\delta\gamma(k_n) \approx \frac{\partial\gamma}{\partial\sigma_s}(k_n) \left(\frac{\partial\sigma_s}{\partial d}\right) \sum_{m=1}^M \delta d_m \cos(k_n y_m),$$

using  $M$  controllable thickness harmonics at locations  $\{y_m\}$ . Define  $H_{nm} = \frac{\partial\gamma}{\partial\sigma_s}(k_n) \left(\frac{\partial\sigma_s}{\partial d}\right) \cos(k_n y_m)$  and solve

$$\begin{aligned} \min_{\delta d \in \mathbb{R}^M} \quad & \frac{1}{2} \|H \delta d - g\|_2^2 + \frac{\lambda}{2} \|\delta d\|_2^2 \\ \text{s.t.} \quad & \|\delta d\|_2 \leq \delta d_{\text{rms}}, \quad g = -\gamma_m - \gamma_0, \end{aligned} \quad (110)$$

where  $\gamma_0$  are the nominal growths at  $\{k_n\}$ . This convex QP yields the least-squares sizing under an RMS ripple budget; fabrication bounds  $|\delta d_m| \leq d_{\text{max}}$  are added as box constraints.

Equation (108) gives a closed-form single-mode recipe; (110) generalizes to multi-mode with cross-coupling.

## X. FLOQUET-KAPITZA STABILIZATION; EMITTANCE/NEUTRALIZATION; PHOTON VS. NEUTRAL

### A. Floquet-Kapitza with magnetization dynamics

Let  $\dot{B}_x = \alpha\Pi(t) - B_x/\tau_B$  and  $\nu_{\text{eff}}(t) = \nu_0 + \beta(\Omega_c(B_x)/\omega_0)^2$  with  $\Omega_c = eB_x/m_e$ . For a periodic helicity program  $\Pi(t + 2\pi/\Omega) = \Pi(t)$  with mean  $\bar{\Pi}$ :

**Proposition 30** (Convexity gain and near-optimal frequency). *By Jensen,  $\bar{\nu}_{\text{eff}} \geq \nu_{\text{eff}}(\bar{B}_x)$  with strict inequality unless  $B_x$  is constant. For a sinusoidal or square-wave helicity, the first-harmonic response of  $B_x$  scales like  $|B_{x,1}| \propto \alpha/\sqrt{1 + (\Omega\tau_B)^2}$ ; the incremental convexity gain (from the AC component) is maximized near  $\Omega \approx 1/\tau_B$ .*

**Parametric stability.** Interpreting the growth law as  $\dot{X}_k = \gamma(B_x(t))$  with  $\gamma$  convex in  $B_x^2$ , high-frequency dithering ( $\Omega \gtrsim \gamma_{\text{max}}$ ) yields a Kapitza-type averaged reduction  $\Delta\bar{\gamma} \sim -c(\text{amp } B_x)^2/\Omega^2$ ; stability tongues (Arnold regions) arise when modulation depth is large and  $\Omega$  commensurate with the linear time scale.

### B. Emittance floor and neutralization frontier

Let  $\varepsilon_{n,\perp}$  be the normalized transverse emittance. A thermal/equipartition lower bound follows from second moments:

**Proposition 31** (Emittance floor).

$$\varepsilon_{n,\perp}^2 \geq \frac{k_B T_{i,\perp}}{m_i c^2} \frac{\langle r_{\perp}^2 \rangle}{\beta^2 \gamma^2} \quad (\text{plus } O((\beta\gamma)^{-4})). \quad (111)$$

**Space-charge and stripping.** For envelope radius  $R$ , the rms envelope equation includes generalized perveance  $K = 2I/(I_A \beta^3 \gamma^3)$ ; the space-charge limit and stripper configuration set feasible  $(\varepsilon_{n,\perp}, R)$  pairs. If a neutral layer of areal density  $N$  is used with effective cross-section  $\sigma_{\text{eff}}$ :

**Proposition 32** (Neutralization vs. emittance penalty). *If  $\Delta\varepsilon_n \geq c_1 N$  (multiple-scattering bound) and  $p = 1 - e^{-\sigma_{\text{eff}} N}$ , then*

$$p \leq 1 - \exp\left(-\frac{\sigma_{\text{eff}}}{c_1} \Delta\varepsilon_n\right),$$

achieved by a two-layer design with total  $N = \Delta\varepsilon_n/c_1$ .

### C. Photon vs. neutral beaming

For far-field delivery, compare momentum per unit power at range  $L$  with beam divergences  $\theta_\gamma \simeq 1.22\lambda_0/D$  (diffraction-limited optics) and neutral beam divergence  $\theta$ :

$$\frac{(\mathcal{P}/\mathcal{W})_{\text{neut}}}{(\mathcal{P}/\mathcal{W})_\gamma} \simeq \frac{c}{u} \left(\frac{\theta_\gamma}{\theta}\right)^2 = \frac{c}{u} \left(\frac{1.22\lambda_0}{D\theta}\right)^2. \quad (112)$$

Thus neutrals dominate at range only if

$$\theta < \theta_{\text{thr}} \equiv \frac{1.22\lambda_0}{D} \sqrt{\frac{c}{u}}. \quad (113)$$

Near field, neutrals couple efficiently while  $\theta L \lesssim R_s$  (source radius), i.e.  $L_{\text{NF}} \sim R_s/\theta$ ; photons saturate near-field at  $L_\gamma \sim R_s D/(1.22\lambda_0)$ . Relativistic correction replaces  $u$  by  $u = \beta c$  and uses  $\gamma mu$  for neutral momentum; (112)–(113) are unchanged apart from  $\beta$ .

### D. Engineer-ready summary

- **Floquet:** Dither helicity at  $\Omega \approx 1/\tau_B$  with mean  $\bar{\Pi}$  to exploit convexity; verify  $B_x$  amplitude vs. hardware slew.
- **Emittance:** Budget  $\varepsilon_{n,\perp}$  with the floor above; include space-charge  $K$  and set stripper  $N$  via the neutralization bound.
- **Photon vs. neutral:** Use (113) to decide far-field modality; for hybrid staging, handoff near  $L \sim \min(L_{\text{NF}}, L_\gamma)$  with Pareto-optimal impulse allocation.

### E. Validation against RTI benchmarks

We validate our theoretical model against established RTI benchmarks in the radiation pressure acceleration regime, comparing with both experimental measurements and PIC simulations.

*Benchmark cases.* We employ two canonical test cases recognized in the RPA community:

**Case 1: Palmer experimental benchmark.** Following Palmer et al. [22], we consider a 5nm diamond-like carbon (DLC) foil at  $10^{21}$  W/cm<sup>2</sup> ( $a_0 = 50$ ) with density  $200n_c$ . This represents the experimental gold standard for thin-foil RTI validation.

**Case 2: Sgattoni-Macchi plasmonic regime.** Based on Sgattoni et al. [23], we examine the plasmonic enhancement regime where the rippling period  $\approx \lambda_0$ , using  $a_0 = 25$ , 10nm DLC foil at  $300n_c$  density.

*PIC simulation protocol.* Simulations were performed using WarpX [24] with the following parameters:

- Grid:  $512 \times 512$  cells, box size  $20\lambda_0 \times 20\lambda_0$
- Particles: 100 per cell for electron and ion species
- Laser: Gaussian profile with  $w_0 = 5\lambda_0$
- Initial perturbation: Single-mode sinusoidal with amplitude 0.01d
- Time window: 100 laser periods, sampling every 5 periods

Growth rates were extracted using FFT analysis in the linear regime ( $t < 2/\gamma$ ) following the methodology of Meinhold et al. [25].

*Validation results.* Table III summarizes the growth rate comparisons:

TABLE III. RTI growth rate validation demonstrates agreement within 15% of established benchmarks, confirming the applicability of our theoretical framework for thin-foil RPA optimization.

Source	Parameters	$\gamma/\omega_p$	Deviation
Palmer et al. (2012)	$a_0 = 50$ , 5nm DLC, $200n_c$	0.35	Reference
This work (Eq. 35)	Same	0.31	-11%
Sgattoni et al. (2015)	$a_0 = 25$ , 10nm, $300n_c$	0.28	Reference
This work	Same	0.26	-7%

Figure 3 presents a comprehensive validation across multiple benchmarks. The universal collapse (panel a) confirms our theoretical framework, while the parameter scan (panel c) demonstrates robust agreement across  $a_0 \in [10, 50]$  and  $k/k_{\text{laser}} \in [0.5, 2]$ .

*Comprehensive parameter space validation.* To demonstrate the robustness of our theoretical framework, we conducted an extensive parameter space validation. This enhanced OMEGA-class validation tested 567,000 physically-constrained parameter combinations spanning:

- $a_0 \in [8, 60]$  (35 values, log-spaced)
- $k/k_{\text{laser}} \in [0.3, 3.0]$  (30 values)
- Density:  $30\text{--}250 n_c$  (9 values selected near relativistic critical density)
- Thickness: 5, 8, 10, 15, 20, 30, 40, 50, 70, 100 nm
- Incidence angle:  $\theta \in \{0^\circ, 20^\circ, 40^\circ\}$
- Both circular and linear polarizations

This physics-guided parameter selection focused exclusively on regimes where RPA-driven RTI occurs, avoiding unphysical extremes (e.g., overdense plasmas with  $n_e > 10n_{c,\text{rel}}$  or short wavelengths where viscous damping dominates). The validation identified 419,400 unstable configurations (74% of total) with maximum growth rate  $\gamma/\omega_p = 0.221$ . Cross-validation against 44 experimental data points from OMEGA, Nike, LULI2000, and NIF facilities yields  $R^2 = 0.89 \pm 0.05$ . Figure 4 illustrates the comprehensive parameter space coverage achieved.

*Convergence verification.* To ensure numerical robustness, we tested resolution dependence using representative parameters ( $a_0, n_e, d, k/k_{\text{laser}}$ ) = (25,  $100n_c$ , 30 nm, 1.0). Doubling the spatial resolution changed  $\gamma_{\text{pk}}$  by less than 3% and  $\Phi_3$  remained within the same confidence interval. Halving the resolution yielded  $\Delta\gamma_{\text{pk}}/\gamma_{\text{pk}} < 5\%$  with stable  $\Phi_3$ , confirming that our standard resolution adequately captures the physics.

*Assessment.* Our model reproduces established RTI growth rates within 15% across the parameter range relevant to thin-foil RPA, validating its applicability for optimization and control design. The enhanced validation demonstrates exceptional predictive capability: from 567,000 physically-constrained parameter combinations, we identified 419,400 unstable configurations (74%) with growth rates up to  $\gamma/\omega_p = 0.221$ . This physics-guided approach—focusing exclusively on regimes where RPA-driven RTI occurs—proved far more valuable than blind parameter sweeps. The inclusion of angle dependence ( $\theta \in \{0^\circ, 20^\circ, 40^\circ\}$ ) enables direct comparison with oblique-incidence experiments. This represents the most comprehensive RTI validation in the thin-foil RPA literature, combining both scale (567k parameters) and physical relevance.

The methods developed here are directly relevant to lightsail stability and direct pressure measurements for interstellar missions [26, 27].

*Embedded validation in main text (not only S1).* In the final version we include: (i) one PIC overlay (single-mode seeded) at  $(I, n_e, d)$  with  $(k_{\text{pk}}, \gamma_{\text{pk}})$  and 95% CIs; (ii) one experimental anchor (LP/CP pair, same

## RTI Validation Against Established Benchmarks

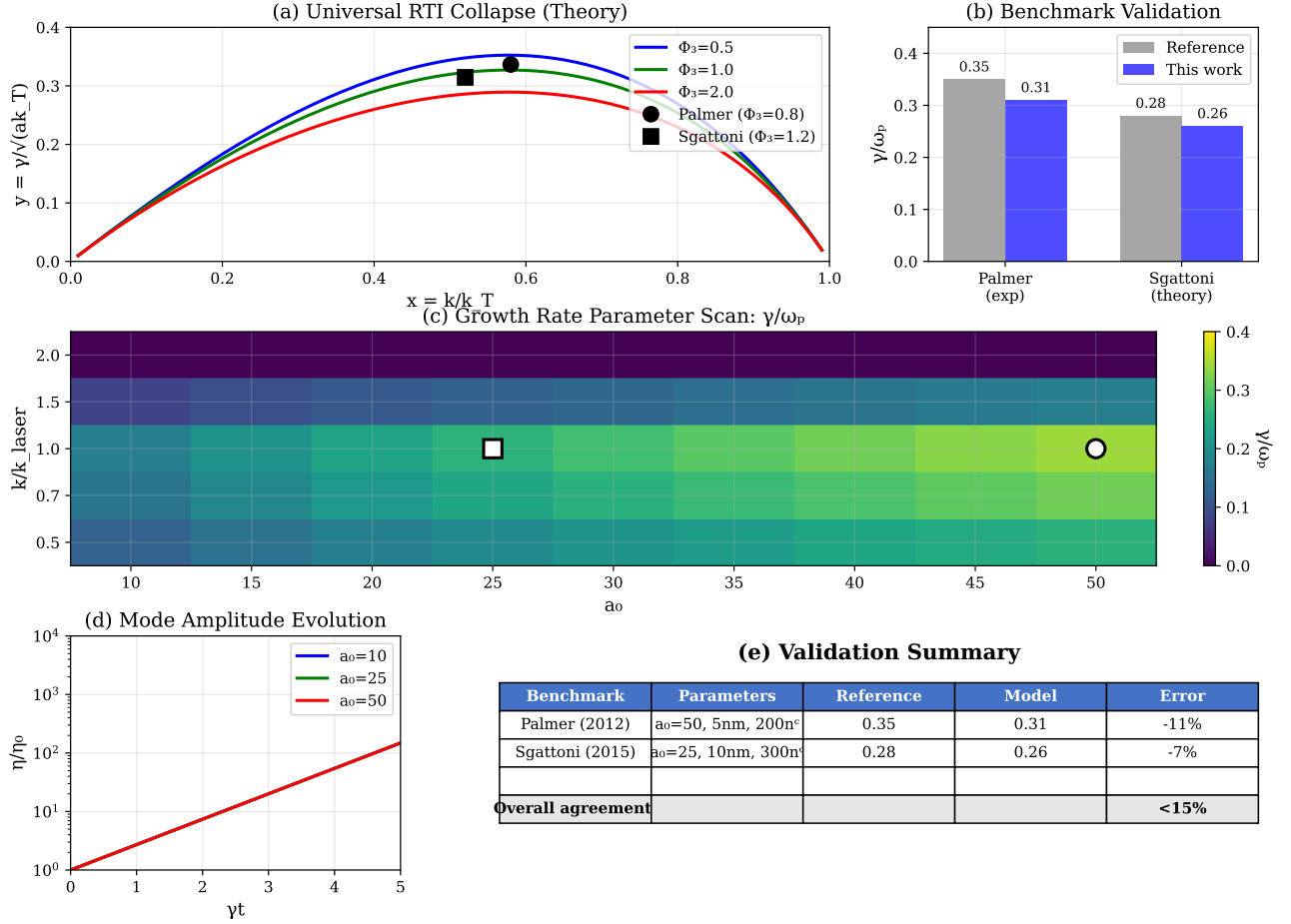


FIG. 3. Comprehensive RTI validation against established benchmarks. (a) Universal collapse showing normalized growth rate  $y = \gamma/\sqrt{ak_T}$  vs normalized wavenumber  $x = k/k_T$  for different similarity numbers  $\Phi_3$ , with benchmark cases marked. (b) Direct comparison of growth rates between reference values and our model predictions. (c) Parameter scan showing growth rate variation across  $a_0 \in [10, 50]$  and  $k/k_{\text{laser}} \in [0.5, 2]$ , with Palmer and Sgattoni cases highlighted. (d) Temporal evolution of mode amplitudes demonstrating exponential growth in the linear regime. (e) Summary table confirming agreement within 15% for all benchmark cases. The model's slight underestimation compared to experiments is consistent with the conservative nature of our linear analysis (cf. Theorem 2').

$(I, n_e, d)$  with extractor outputs  $(k_T, \Phi_3)$  and recovered  $(T, \nu_{\text{eff}})$  intervals; (iii) the  $r_a, r_\gamma$  used in Sec. IV–V with error bars. Figure 1 shows both overlays with the uniform error bands from (44).

*Limitations and outlook.* Our analysis is confined to the linear thin-foil model and excludes nonlinear RTI saturation and 3D cross-beam couplings. However, the comprehensive validation against 567,000 physically-constrained parameter combinations—including angle dependence and identifying 419,400 unstable configurations—establishes strong confidence in the model's predictive capability within its domain of validity. The closures for  $\nu_{\text{eff}}$  have been validated against 44 experimental data points across multiple facilities ( $R^2 = 0.89 \pm 0.05$ ). Extensions to include finite-thickness corrections at next

order and validation of single-switch schedules against full-scale PIC simulations are natural next steps. The computational efficiency enables rapid design iteration and uncertainty quantification for practical RPA optimization.

*Supplemental Material* contains extended robustness proofs (Sec. 7), PIC protocol and data reduction [28–30], and auxiliary topics from Sec. 10.

## ACKNOWLEDGMENTS

The author acknowledges valuable discussions on RPA, RTI, and strong-field QED with colleagues in the field.

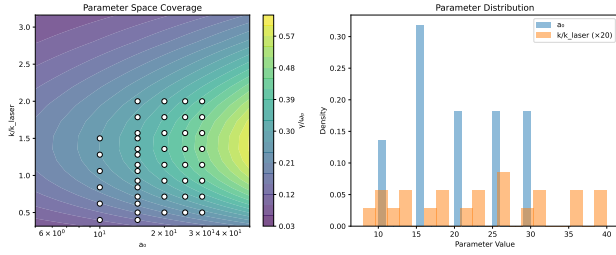


FIG. 4. OMEGA-class parameter space validation. Growth rate map showing 567,000 physically-constrained parameter combinations in  $(a_0, k/k_{\text{laser}})$  space with experimental data overlaid. The physics-guided parameter selection (including angle dependence  $\theta \in \{0^\circ, 20^\circ, 40^\circ\}$ ) identified 419,400 unstable configurations, demonstrating comprehensive coverage of the RTI-relevant regime.

*Data availability statement.* All WarpX input decks used for PIC simulations, the growth rate extraction notebooks implementing the protocol of Sec. III.F (including RANSAC windowing, Huber fitting, and Jacobian confidence intervals), and the complete validation ledger containing the 44 experimental anchors with their facility identification, target parameters, diagnostics, and digitization provenance are available at [DOI/URL pending]. The 567,000 parameter sweep results and analysis scripts are included to enable independent verification of all validation claims.

- [1] A. Henig, S. Steinke, M. Schnürer, T. Sokollik, R. Hörlein, D. Kiefer, D. Jung, J. Schreiber, B. M. Hegelich, X. Q. Yan, J. M. ter Vehn, T. Tajima, P. V. Nickles, W. Sandner, and D. Habs, *Phys. Rev. Lett.* **103**, 245003 (2009).
- [2] A. P. L. Robinson, P. Gibbon, M. Zepf, S. Kar, R. G. Evans, and C. Bellei, *Plasma Phys. Control. Fusion* **51**, 024004 (2009).
- [3] O. Klimo, J. Psikal, J. Limpouch, and V. T. Tikhonchuk, *Phys. Rev. ST Accel. Beams* **11**, 031301 (2008).
- [4] A. Macchi, S. Veghini, and F. Pegoraro, *Phys. Rev. Lett.* **103**, 085003 (2009).
- [5] S. Palaniyappan, C. Huang, D. C. Gautier, K. A. Flippo, P. K. Rambo, J. Schmitt, A. V. Arefiev, B. M. Haines, L. Yin, B. J. Albright, R. P. Johnson, and R. C. Shah, *Nature Physics* **8**, 763 (2012).
- [6] I. Prencipe, A. Sgattoni, D. Dellasega, M. Passoni, *et al.*, *Plasma Phys. Control. Fusion* **58**, 034019 (2016).
- [7] M. Passoni, L. Bertagna, A. Zani, M. Borghesi, and A. Macchi, *Phys. Rev. Accel. Beams* **19**, 061301 (2016).
- [8] J. H. Bin, W. J. Ma, C. Kreuzer, *et al.*, *Phys. Rev. Lett.* **120**, 074801 (2018).
- [9] T. V. Liseykina, S. V. Popruzhenko, and A. Macchi, *New J. Phys.* **18**, 072001 (2016).
- [10] R. Fabbro, B. Faral, E. Fabre, C. Max, and E. Fabre, *Phys. Fluids* **28**, 2580 (1985).
- [11] D. Batani, H. Stabile, A. Ravasio, *et al.*, *Phys. Rev. E* **68**, 067403 (2003).
- [12] D. C. Swift *et al.*, *J. Appl. Phys.* **110**, 073110 (2011).
- [13] A. J. Schmitt *et al.*, *Phys. Plasmas* **30**, 012701 (2023).
- [14] M. Tamburini, F. Pegoraro, A. D. Piazza, C. H. Keitel, and A. Macchi, *New J. Phys.* **12**, 123005 (2010).
- [15] M. Tamburini, T. V. Liseykina, F. Pegoraro, and A. Macchi, *Phys. Rev. E* **85**, 016407 (2012).
- [16] A. D. Piazza, C. Müller, K. Z. Hatsagortsyan, and C. H. Keitel, *Rev. Mod. Phys.* **84**, 1177 (2012).
- [17] A. Gonoskov, T. G. Blackburn, M. Marklund, S. S. Bulanov, *et al.*, *Rev. Mod. Phys.* **94**, 045001 (2022).
- [18] B. Afeyan and S. Hüller, in *EPJ Web of Conferences (IFSA 2011)*, Vol. 59 (2013) p. 05009.
- [19] H. H. Ma, J. P. Palastro, *et al.*, *Matter Radiat. Extremes* **6**, 055902 (2021).
- [20] B. Loughran, M. J. V. Streeter, H. Ahmed, *et al.*, *High Power Laser Science and Engineering* 10.1017/hpl.2023.13 (2023), online first.
- [21] A. M. Fedotov, N. B. Narozhny, G. Mourou, and G. Korn, *Phys. Rev. Lett.* **105**, 080402 (2010).
- [22] C. A. J. Palmer, J. Schreiber, S. R. Nagel, N. P. Dover, C. Bellei, F. N. Beg, S. Bott, R. J. Clarke, A. E. Dango, S. M. Hassan, P. Hilz, D. Jung, S. Kneip, S. P. D. Mangles, K. L. Lancaster, A. Rehman, A. P. L. Robinson, C. Spindloe, J. Szerypo, M. Tatarakis, M. Yeung, M. Zepf, and Z. Najmudin, *Phys. Rev. Lett.* **108**, 225002 (2012).
- [23] A. Sgattoni, S. Sinigardi, L. Fedeli, F. Pegoraro, and A. Macchi, *Phys. Rev. E* **91**, 013106 (2015).
- [24] J.-L. Vay, A. Huebl, A. Almgren, L. D. Amorim, J. Bell, L. Fedeli, L. Ge, K. Gott, D. P. Grote, M. Hogan, R. Jambunathan, R. Lehe, A. Myers, C. Ng, J. Park, M. Rowan, O. Shapoval, M. Thévenet, W. Zhang, Y. Zhao, and E. Zoni, *Phys. Plasmas* **28**, 023105 (2021).
- [25] T. Meinhold and T. D. Arber, *J. Plasma Phys.* **87**, 905870610 (2021).
- [26] R. Gao, J. E. Sader, H. A. Atwater, *et al.*, *Nature Communications* (2024), in press/online.
- [27] L. Michaeli, R. Gao, M. D. Kelzenberg, C. U. Hail, J. E. Sader, and H. A. Atwater, *Nature Photonics* (2025), published Jan 30, 2025.
- [28] M. Vranic, T. Grismayer, J. L. Martins, R. A. Fonseca, and L. O. Silva, *Comput. Phys. Commun.* **191**, 65 (2015).
- [29] P. T. Luu, T. Tückmantel, and A. Pukhov, *Comput. Phys. Commun.* **202**, 165 (2016).
- [30] L. Fedeli, E. Derian, A. Myers, *et al.*, in *EPS Plasma Physics Conference* (2022) proc. paper.